Article

On Street-Canyon Flow Dynamics: Advanced Validation of LES by Time-Resolved PIV

Radka Kellnerová [1,†,*] [ID], **Vladimír Fuka** [2,‡] [ID], **Václav Uruba** [1,‡], **Klára Jurčáková** [1,‡] [ID], **Štěpán Nosek** [1,‡] [ID], **Hana Chaloupecká** [1,2,‡] and **Zbyněk Jaňour** [1,‡] [ID]

1   Institute of Thermomechanics CAS, v.v.i., Dolejskova 1402/5, 182 00 Prague 8, Czech Republic; uruba@it.cas.cz (V.U.); klara.jurcakova@it.cas.cz (K.J.); nosek@it.cas.cz (S.N.); hanach@it.cas.cz (H.CH.); janour@it.cas.cz (Z.J.)
2   Faculty of Mathematics and Physics, Department of Atmospheric Physics, Charles University in Prague, V Holesovickach 2, 180 00 Prague 8, Czech Republic; vladimir.fuka@mff.cuni.cz
*   Correspondence: radka.kellnerova@it.cas.cz; Tel.: +420-266-053-202
†   Current address: Institute of Thermomechanics CAS, v.v.i., Dolejskova 1402/5, 182 00 Pragu 8, Czech Republic.
‡   These authors contributed equally to this work.

check for updates

Abstract: The advanced statistical techniques for qualitative and quantitative validation of Large Eddy Simulation (LES) of turbulent flow within and above a two-dimensional street canyon are presented. Time-resolved data from 3D LES are compared with those obtained from time-resolved 2D Particle Image Velocimetry (PIV) measurements. We have extended a standard validation approach based solely on time-mean statistics by a novel approach based on analyses of the intermittent flow dynamics. While the standard Hit rate validation metric indicates not so good agreement between compared values of both the streamwise and vertical velocity within the canyon canopy, the Fourier, quadrant and Proper Orthogonal Decomposition (POD) analyses demonstrate very good LES prediction of highly energetic and characteristic features in the flow. Using the quadrant analysis, we demonstrated similarity between the model and the experiment with respect to the typical shape of intensive sweep and ejection events and their frequency of appearance. These findings indicate that although the mean values predicted by the LES do not meet the criteria of all the standard validation metrics, the dominant coherent structures are simulated well.

Keywords: wind tunnel; LES; validation; street canyon; coherent structures

1. Introduction

Numerical codes for computational fluid dynamics (CFD) have been developed and used in industrial CFD applications where a variety of practical problems are predicted and tested (e.g., [1]). Owing to the enormous complexity of turbulence and extremely variable boundary conditions, the modelling of the micro-meteorological scale has been delayed with respect to their practical implementations. After years of intensive development, the numerical codes for near-surface atmospheric flow have attained a level of sufficient precision in mathematical description and spatial resolution. Time-resolving frameworks, such as Large-Eddy Simulation (LES) and Direct Numerical Simulation (DNS), have the potential now to become truly credible calculation tools for solving air quality issues since these models are capable of capturing the time-dependent behaviour of turbulence.

The CFD model needs to undergo a thorough validation procedure before its practical implementation. The validation determines to what extent the model is in agreement with real physics. An extensive review of the evaluation methodologies as well as the definition of the nomenclature used can be found in Oberkampf and Trucano [2].

For turbulent boundary-layer flow problems, the best data sources are field measurements. Unfortunately, field measurements are very rarely available and, as Schatzmann and Leitl [3] pointed out, the micro-meteorological flow found in field measurements exhibits much larger scatter than the data from a closely-controlled wind-tunnel experiment. Therefore, field data represent a greater challenge in terms of post-processing and preparation for a validation. Thus, the CFD results are often compared with those from wind-tunnel experiments [4–9]. That said, the CFD validations against data from street-canyon field experiments were performed as well (e.g., [10–12]).

A validation procedure for atmospheric boundary layer dispersion or velocity distribution predictions by CFD was compiled within the frame of COST 732 [13–15], COST C14 [16] and AIJ Tominaga et al. [17]. These guidelines addressed various types of models including Gaussian models, and RANS and LES models. The latter, LES model, represents an affordable combination of direct simulation of large turbulent structures while modelling small unresolved scales by means of an embedded sub-grid model [18].

Since common validation techniques target just the variables that are available from all the discussed models, only temporally-averaged values are usually retrieved for comparison. Illustrative applications of the validation of temporally-averaged values from LES against various experiments can be found in Jimenez and Moser [18]. The most suitable experimental data currently available are those obtained from Particle Image Velocimetry (PIV) measurement techniques as they can provide multi-points time-resolved synchronised data. The use of PIV for the validations is, however, still rare [4,19,20]. Since there may be a lack of a sufficiently long time period from LES or from PIV to achieve legitimate statistical averages, a feasible strategy for the validation of LES is, according to Hertwig et al. [20], not only the comparison of mean values but also a multi-point time-series analysis by means of advanced statistical tools, which allows us to detect transient structures, their shape and also frequency distribution.

In this paper, we present an extension of a validation procedure introduced by the research of [20–22] and Hertwig [23], in which a three-level validation hierarchy, consisting of global statistics, eddy statistics and flow structure statistics was employed. The extension comprises time-series analyses such as the spectral and spatial modification of the quadrant analysis, and the temporally-spatial analyses, namely the spatial correlation or the Proper Orthogonal Decomposition (POD). By this extension, we demonstrate that spatial data from the time-resolved particle image velocimetry (TR-PIV) improve the validation procedure. As suggested in Jimenez and Moser [18], the Reynolds stress is also a very sensitive quantity for testing the LES sub-grid model. Hence we present the investigation of the momentum flux by an additional spatial quadrant analysis as well.

This strategy respects the time-dependent nature of the coherent features and reveals the similarity between the predicted and measured turbulent flow in a more detailed manner. Our goal is to validate the capability of the LES to simulate both the larger-scale coherent features above the canyon, known to be crucial for street canyon ventilation (e.g., [7,24–26]), and to model the small-scale swirls, responsible for the intense mixing process inside the street canyon itself (e.g., [6]). Strengths and shortcomings of the well-established validation metrics are thoroughly discussed and the benefits of the innovative methods are introduced.

2. Methods and Data Pre-Processing

2.1. Experimental Method

The experiment was performed in a pressure-driven open-circuit wind tunnel with a test section of cross-sectional dimensions 0.25×0.25 m and a length of 3 m. A fan, followed by a 3 m long tunnel duct and a contraction pipe, was installed upstream of the test section. The street-canyon model covered the entire test section. The model was built from 30 identical parallel street canyons, spanned laterally across the width of the tunnel (0.25 m). The building height and the roof height was 0.03 m

and 0.02 m, respectively. The aspect ratio of the street canyon (street-canyon height $H = 0.05$ m to street-canyon width W) was equal to one $H/W = 1$ (Figure 1).

The triangular shape of the street-building roofs was chosen according to roofs typical for European city centres. Kellnerova et al. [24] pointed out that triangle roofs generate more turbulent dynamics than flat ones and to successfully validate the flow behind the triangle roofs is therefore more challenging. The presented experimental set-up was a part of the measurement campaign comparing a skimming flow and its dynamics between street canyons with the flat and pitched roofs in a neutrally stratified boundary layer flow. A detailed description of the campaign can be found in Kellnerova et al. [24] or Kellnerova [27].

The PIV measurements were taken downstream behind the 20th street canyon and only at the tunnel axis in order to guarantee a fully developed flow and to avoid a wall effect. Based on an empty wind-tunnel measurement, the wall affects the mean velocity in distances up to 40–60 mm from the walls. Although we do not consider the boundary layer above the street canyons as fully representative of the atmospheric flow due to the excessive aerodynamical blocking caused by buildings (achieving value of 20%), the lowest part of the boundary layer shows significant similarity with a true atmospheric layer in terms of normalised lower and higher moments and cross-moments of the velocity [27]. The numerical large-eddy simulation copies the cross-sectional test section dimension and simulates the aforementioned effects of the walls.
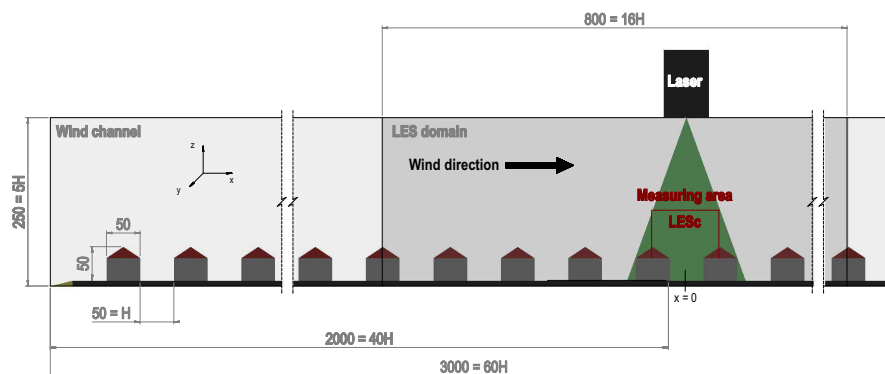

Figure 1. Isometric view of the model positioned in the tunnel test section. The measured area by TR-PIV system is indicated by the red rectangle within the green laser sheet. The dimensions are in mm.

The wind-tunnel coordinate system (x, y, z) corresponds to the streamwise (u), lateral (v) and vertical (w) instantaneous velocity, where the mean velocity components are labelled U, V and W, and their fluctuations according to Reynolds decomposition, as u', v' and w'. The mean wind speed measured above the street-canyon centre $(x/H = 0, z/H = 2)$ was $U_{2H} = 5.7$ ms^{-1}. Thus, the Reynolds building number became $Re_{2H} = U_{2H}H/\nu = 19\,000$, where ν is the kinematic viscosity of the air. The velocity measurements were conducted with the TR-PIV system, providing 2-D snapshots of the instantaneous velocity vectors in a single streamwise-vertical plane (xz) placed 2000 mm (40 H) downstream from the test section entrance (see Figure 1). One run of PIV measurements consisted of 1634 image-pairs. An overview of the PIV parameters is listed in Table A1 in Appendix A.

Additional measurements above the height of $z/H = 1$ were performed by means of CTA hot-wire anemometry (HWA), with a single-wire probe DANTEC 55P01 (tungsten wire with a diameter of 0.005 mm and a length of 1.25 mm). The HWA provided a sampling frequency of 25 kHz for the 1-dimensional streamwise velocity component u. Prior to the validation procedure, the HWA velocity data were compared with the PIV data in terms of the mean velocity, turbulence intensity, skewness, flatness, histogram and spectra for the streamwise velocity component. Good agreement was found in all cases [27]. The spanwise homogeneity of the mean velocity was 2.3%. The HWA system reached a very good accuracy of 1% for the streamwise velocity component.

2.1.1. Numerical Method

For this study, we used the LES model called the Charles University Large-eddy Microscale Model (CLMM) developed by Fuka [28]. CLMM is an in-house finite difference solver of the incompressible Navier-Stokes equations that uses LES to model the smallest scales in the flow. The code uses uniform staggered Cartesian grids. Solid obstacles are treated by using the immersed boundary method [29,30].

CLMM uses implicit filtering, i.e., it is assumed that the variables are filtered by using approximate numerical schemes on a finite grid. The solution of the discrete Poisson system is performed using the open source library PoisFFT [28]. The spatial derivatives are computed using the second-order central differences with the exception of the momentum advection, which is computed using the fourth-order central differences [31] that reduce to second order differences in cells closest to the wall. The discrete system is integrated usign the 3rd order Runge-Kutta method with variable time step keeping the Courant number below 0.9.

The subgrid scale eddy viscosity is computed by the σ-model by Nicoud et al. [32] and the shear stresses on solid walls are computed using a wall model with a logarithmic wall function when the wall coordinate is $y^+ > 11.2$. The wall model uses the instantaneous velocity in the closest gridpoint to compute the shear stress. The wall coordinate y^+ was lower than 30 in this simulation.

For this study the model was run on a uniform grid with a constant resolution of 2 mm in each direction. The boundary conditions of the model follow the boundary conditions of the wind-tunnel test section as much as possible. The vertical and lateral dimensions of the wind tunnel are fully solved by LES over the whole extent (5 H of both vertical and lateral direction) with the no-slip boundary conditions on the tunnel walls. The streamwise dimension covers the length of 16 H (0.26 of the full test-section length). Cyclic boundary conditions were specified only in the x-direction for the upstream and downstream boundaries, and therefore the model represents an infinite number of idealised street canyons along the streamwise direction. A detailed description and the principal equations can be found in Appendix B.

3. Data Pre-Processing

For the LES validation procedure, we performed two levels of data analyses. The first level comprises a qualitative and quantitative comparison between the temporally and spatially averaged quantities of the wind-tunnel experiment and the LES model by means of profiles and standard validation metrics. The second level represents comparisons of intermittent flow dynamics between the experiment and the LES model by means of well-established statistical methods for detection of the turbulent coherent structures (spectral and quadrant analysis, correlation and POD). For each analytical approach, we performed a specific data pre-processing procedure.

3.1. Analyses of Time-Averaged Flow

All of the velocity data were normalized by the reference velocity, U_{ref}, which was temporally and horizontally averaged along the streamwise direction at the reference height ($x/H \in [-0.5, 0.5]$, $H_{ref} = z/H = 1.5$), where the LES data as well as the PIV data were available. The HWA measurement was conducted at the canyon centre and the reference velocity was achieved at a single point ($x/H = 0$, $H_{ref} = z/H = 1.5$). The temporal scale was converted into the dimensionless time, t^*, based on the formula [33]

$$t^* = t \frac{U_{ref}}{H_{ref}} \tag{1}$$

where t is the real or simulated time during the experiment or LES simulation, respectively.

For the time-mean analysis, all the experimental and numerical data available were gathered and averaged. The data from three PIV runs, each containing 1634 snapshots, were combined into one ensemble with 4902 snapshots in total, labelled PIVa. The total dimensionless time corresponds to $t^*_{PIVa} = 1295$. All LES computational periods were equal to 18 s and steady-state results were obtained

from the last 10 s of the computations. Since the cyclic boundary conditions were implemented at the inlet and outlet of the domain boundaries, the streamwise position of the individual canyons did not matter. The overall statistics of the LES data were derived from the temporal and spatial averaging across all eight canyons and are labelled LESa. By assembling this large database, the effective simulation time increased to a value of t_a =80 s and the number of snapshots reached 80,000. The dimensionless total time became $t^*_{LESa} = 1528$.

3.2. Analyses of Intermittent Flow

For validation of the simulated time-dependent flow dynamics, we used the continuous time-resolved measurements from the PIV run (labelled PIVc) with the following parameters: 1634 snapshots, $t_c = 3.2$ s, $t^*_{PIVc} = 181$. The continuous HWA time-series (the streamwise velocity only, labelled HWAc) were recorded over $t_c = 30$ s, and corresponded to $t^*_{HWAc} = 1704$, respectively. For the continuous time-resolved LES data (labelled LESc), the time-series lasting $t_c = 10$ s and $t^*_{LESc} = 191$ from one canyon were employed in the validation procedures concerning the flow dynamics.

The grid resolution of the PIV data is finer (1.2 mm) than the LES resolution (2 mm). For the purpose of the validation, we started to prepare a systematic comparison between the different grid resolutions of the LES. Based on the very preliminary, not-yet-published results from the LES with half resolution (1 mm), the number of grid points, P, is considered by the authors of this paper to have a crucial impact on the LES performance. An overview of the methodology regarding the set-ups for PIV and LES is presented in Table 1.

Table 1. Parameters of the methodologies HWA, PIV and LES.

Measurement Methodology	HWA	PIV	LES
Number of samples/snapshots	750,000	4902	10,000
Spatial resolution [mm]	5	1.2	2
Sampling frequency [kHz]	25	0.5	1
Acquisition time t_a (averaged) [s]	30	22.7	80
Dimensionless time t^*_a (averaged) [-]	1704	1295	1528
Acquisition time t_c (intermittent) [s]	-	3.2	10
Dimensionless time t^*_c (intermittent) [-]	-	181	191

3.3. Measurement Uncertainty

It is common practice to determine the *uncertainty* (also referred to as the measurement error) by means of the standard deviation (STD) of many repeated measurements at reference points. Unfortunately, obtaining a high number of repetitions with PIV requires large data storage. Therefore, only a few runs are usually executed with the PIV system. We repeated the PIV measurement three times. Two measurement runs lasted 3.2 s with a sampling frequency of 500 Hz in order to capture the transient flow dynamics. A third run was performed in order to acquire turbulence statistics and lasted 16.3 s with a low sampling frequency of 100 Hz. The detailed specification of the variation observed between the individual runs is inserted in Appendix C.

Due to the occurrence of spurious vectors just next to the solid walls and edges of the area measured by PIV, the outmost grid points were omitted in the validation metric procedures, which will be discussed later in Section 4.3. We determined the measurement error from the PIV measurements as the spatial average of the STD within the remaining *restricted rectangular area* inside the street canyon. The spatially-averaged STD of the given dimensionless quantities from three PIV samples, the streamwise and vertical velocity component, U/U_{ref} and W/U_{ref}, the momentum flux, $< u'w' > /U^2_{ref}$, and the reduced turbulent kinetic energy, $TKE/U^2_{ref} = 0.5(< u'^2 > + < w'^2 >)/U^2_{ref}$, are listed in Table 2. These values also serve as the absolute deviation criterion for the Hit rate validation procedure discussed in Section 4.3.1.

Table 2. Measurement error expressed as spatially-averaged standard deviation of the given dimensionless quantity (used as the Hit rate absolute deviation criterion A in Section 4.3.1).

Quantity X	Measurement Error (Used as A)
U/U_{ref}	0.008
W/U_{ref}	0.007
$< u'w' > /U_{ref}^2$	0.002
TKE/U_{ref}^2	0.003

4. Results: Model Performance Assessment for Time-Averaged Flow

4.1. Profiles

The vertical profiles of the dimensionless mean streamwise velocity, U/U_{ref}, at the centre of the street canyon are compared in Figure 2a, where the PIVa data are displayed with the horizontal bars representing the measurement error derived from the STD at each elevation. The PIVa (*black squares*) and HWA (*grey squares*) data match remarkably well with the output from LESa for the upper part of the streamwise velocity profile, i.e., within the interval $0.9 < z/H < 1.5$. The lower part is predicted less successfully since the LES model fails to capture properly the exact shape of the recirculation zone inside the canyon, owing to an underestimation of the negative streamwise velocities near the canyon bottom. These discrepancies in the velocity and the corresponding momentum flux deviation plays a significant role in the recirculation vortex pattern, as will be shown later.

The simulated vertical velocity, W/U_{ref}, deviates from the measured one inside the street canyon ($0 < z/H < 0.8$), but agrees well at the roof level (Figure 2b). Likewise, the simulated dimensionless reduced turbulent kinetic energy, $TKE/U_{ref}^2 = 0.5(< u'^2 > + < w'^2 >)/U_{ref}^2$, and the vertical momentum flux, $< u'w' > /U_{ref}^2$, of LESa exhibited very good agreement with those from PIV (Figure 2c,d) within the upper canyon ($0.5 < z/H < 1.5$). The peak of reduced TKE at $z/H = 1.1$ in Figure 2d is predicted extremely well. The peak of momentum flux was slightly overestimated by LESa in terms of magnitude, but mostly within the range of the PIV measurement error. A noticeable discrepancy appears in the lower part of the momentum flux profile ($0.3 < z/H < 0.4$ in Figure 2c). As will be explained later, this positive increase in the total momentum flux in Figure 2c relates to the formation of secondary vortices inside the street.
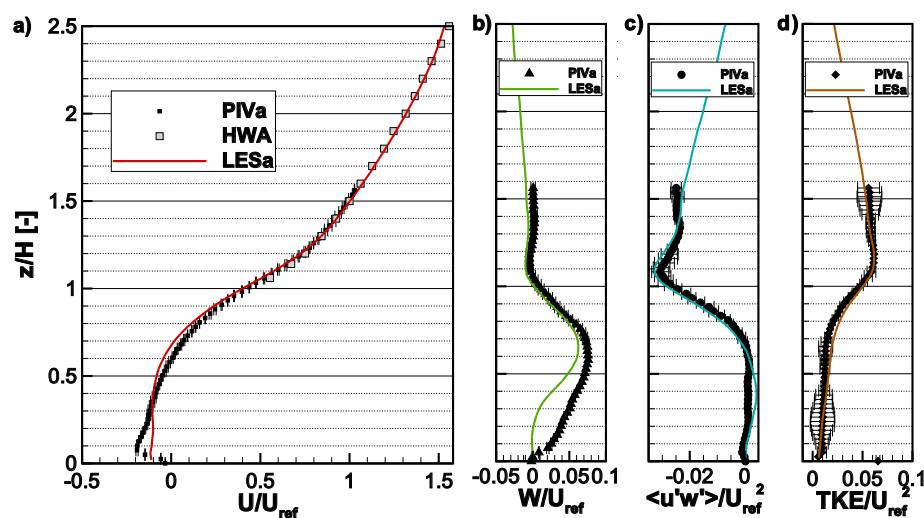

Figure 2. Comparison of the profiles of the mean dimensionless (**a**) streamwise and (**b**) vertical velocities, (**c**) momentum flux and (**d**) reduced turbulent kinetic energy at the centre of the street canyon ($x/H = 0$). The solid lines represent the LES simulation; the symbols denote the wind-tunnel experiment.

4.2. Velocity and Momentum Flux Fields

The mean velocity xz fields for both the streamwise and the vertical velocity, and for the corresponding momentum flux, are depicted in Figure 3a,b. The first line shows the results from the PIVa, and the second line represents the LESa performance. All quantities are normalised by the reference velocity U_{ref}.

Generally, the streamline pattern exhibits a single vortex with the core slightly shifted upward and downstream, compared to the flat roof case [27,34]. This matches previous wind-tunnel studies (e.g., [35,36]) and CFD studies (e.g., [34]) since the exact position depends strongly on either the specific roof geometry [37] or the roof aspect ratio (the roof height to the building width) (e.g., [34]).

A comparison between the dimensionless fields of PIVa (Figure 3a) and LESa (Figure 3b) shows a very good agreement in the region above the street canyon, but a less successful agreement in the region inside the canyon. The streamlines presented in the first column of Figure 3a,b show that LESa predicts a single primary vortex of similar shape as the observed one. The position of the primary vortex centre is predicted by LESa slightly higher compared to PIVa. Further, the secondary windward bottom-corner counter-rotating vortex in the street canyon is over-predicted by the LES model whereas the leeward bottom-corner vortex is completely missing in the simulation (see right and left bottom of the street canyon in Figure 3aI,bI).
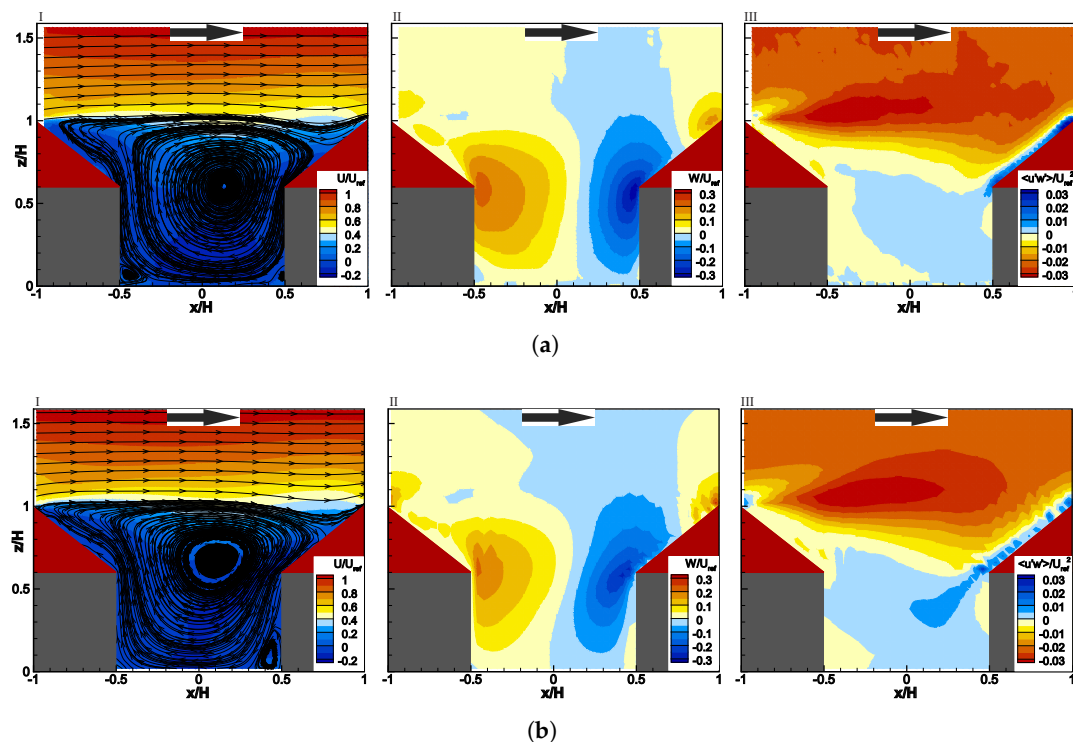

(a)

(b)

Figure 3. The mean dimensionless streamwise velocity with streamlines (first column) and vertical (second column) velocity, and momentum flux (third column) for (**a**) PIVa; and (**b**) LESa.

This corresponds with the notably streamwisely tilted pattern of the simulated vertical velocity field in the second column of Figure 3b, compared to the experiment. Another important observation can be interpreted from the fields of the momentum flux (third column in Figure 3a,b), namely the LES very well predicts the vortex shedding in the roof-top region but it over-predicts the positive streamwise momentum flux within the canyon. As will be shown later in Section 5.3, the vortex in the roof-top region is part of a rather large-scale and smooth up-roof flow, which is well simulated by the LES in general. The zone inside the canyon, on the other hand, consists of many small vortices and shear patterns under the spatial resolution of the LES grid.

4.3. Validation Metrics

A set of general performance metrics to quantitatively assess the agreement between a model and an observation was established by the U.S. Environmental Protection Agency [38] to provide a common framework for various air dispersion model comparisons. The metrics were designed to compare the concentration values by means of their mean or maximum values; they specifically target statistical quantiles and percentiles in order to assess the performance of the model. Only some of the metrics were selected for this paper. Since we work solely with velocity-based data, we modified the following formulae with respect to the used quantities X ($X = U, W, < u'w' >, TKE$):

Fractional bias (FB):

$$\mathbf{FB} = 2\frac{\overline{X_e} - \overline{X_m}}{\overline{X_e} + \overline{X_m}} \tag{2}$$

Root normalised mean square error (RNMSE):

$$\mathbf{RNMSE} = \sqrt{\frac{\overline{(X_e - X_m)^2}}{\overline{X_e}\,\overline{X_m}}} \tag{3}$$

Geometric mean bias (MG) and geometric variance (VG):

$$\mathbf{MG} = exp\left(\overline{\ln X_e} - \overline{\ln X_m}\right), \mathbf{VG} = exp\left[\overline{(\ln X_e - \ln X_m)^2}\right] \tag{4}$$

Pearson correlation (r):

$$\mathbf{r} = \overline{\frac{X_e - \overline{X_e}}{\sigma_e}\,\frac{X_m - \overline{X_m}}{\sigma_m}} \tag{5}$$

where the subscripts e and m refer to the *experiment* and *modelled* data, respectively, $\overline{X}$ denotes the space-averaged value of the time-mean quantity over the restricted rectangular area and the angle bracket $X = \langle x \rangle$ denotes the time-averaged value at a point.

The application of FB, RNMSE, MG and VG to values achieving both positive and negative values can lead to a non-physically-justified experiment-simulation agreement since those values can compensate each other in Equations (2)–(5) as pointed out by Schatzmann et al. [15]. The visual comparison of the data (Figure 3) shows that there is no area where the experimental and modelled data differ in the sign and have a non-dimensionless magnitude higher than 0.1. Therefore, the authors applied those metrics to the absolute values of the investigated quantities with the awareness that the results of the metrics are affected by this phenomenon, but not significantly. An overview of these general metrics is listed in Table 3. The bold values denote the satisfaction of the particular criterion listed in the third column.

The general validation metrics are successfully satisfied in all cases. In comparison with the qualitative validation previously done on the velocity fields, the quantitative validation by means of the general metrics shows a surprisingly good agreement between PIVa and LESa. The main explanation could be that the general metrics work with fixed threshold values, which are not based on the uncertainty of the experimental data, and which were originally proposed for the concentration values. The velocity data more easily comply with these not-so-stringent criterion thresholds. We propose, at least for the Pearson correlation coefficient, that the acceptance criterion should be 0.9 instead of 0.8. The uncertainty itself can be introduced via the *Hit rate* metric, specifically designed by VDI's guidelines for validations of predicted mean velocity fields.

Table 3. General metrics applied to PIVa and LESa.

Metric	Ideal	Accepted	U/U_{ref}	W/U_{ref}	$<u'w'>/U_{ref}^2$	TKE/U_{ref}^2
FB	0	$\in(-0.3,0.3)$	**0.029**	0.209	**0.028**	**0.023**
RNMSE	0	$<\sqrt{1.5}$	**0.005**	0.175	**0.010**	**0.012**
MG	1	$\in(0.7,1.3)$	**1.097**	**1.194**	**0.824**	**1.023**
VG	1	<4	**2.001**	**3.707**	**2.657**	**1.067**
r	1	>0.8	**0.996**	**0.940**	**0.990**	**0.983**

The bold values denote the satisfaction of the particular criterion listed in the third column.

4.3.1. Hit Rate

The Hit rate metric applied in guideline VDI [39] for the validation of prognostic micro-scale wind-field models was used in order to quantitatively compare the experimental and modelled results. The Hit rate metric, q, is calculated by the equation using the normalised numerical model data M_i (modelled) and the normalised observed data E_i (experiment) as

$$q = \frac{1}{P}\sum_{i=1}^{P} q_i \quad \text{with} \quad q_i = \begin{cases} 1 & \text{for} \quad |\frac{M_i - E_i}{E_i}| \leq D \quad \text{or} \quad |M_i - E_i| \leq A \\ 0 & \text{else} \end{cases} \tag{6}$$

where D and A represent the relative and absolute deviation, respectively, according to the guidelines [15,39], with P being the number of grid points within the restricted rectangular area. The Hit rate absolute deviation value, A, was attributed to the normalised measurement error obtained from the given quantity (see Table 2). The relative deviation limit $D = 0.25$ was adopted from Schatzmann et al. [15]. Both acceptance levels A and D are presented in the scatter plots in Figure 4 along with each quantity.

The algorithm (6) is applied to a limited region ($-0.5 < x/H < 0.5$; $0 < z/H < 1.5$). The LES computed grid (1120 spatial points) was fitted to the PIV measured grid (2400 points) by a bilinear interpolation in order to provide one unified spatial domain. The interpolation error was evaluated from a mutual comparison of the linear, cubical and spline version of the interpolating MATLAB procedure applied to typical comparative quantities U, W, $<u'w'>$ and reduced TKE. During the interpolation the values at the points located within the buildings were artificially set to zero. This resulted in lower interpolated values just next to the walls in comparison with those measured by the PIV. The points next to the wall were, however, excluded from Hit rate and other metrics. The difference between the type of interpolations achieved a normalised value of 0.0001. Therefore, the interpolation error is not involved in the absolute value of A.

The final Hit rate values between the LES simulation of the inter-canyons averaged data (labelled LESa) and the averaged values of the repeated experiments (PIVa) are listed in Table 4. Again, the bold values meet the acceptance criterion of **0.66** as defined in VDI [39] for each velocity component. We adopted this criterion in agreement with other studies (e.g., [15,20]) for all the investigated quantities.

Based on the numbers in Table 4, our LES simulation fails to simulate the mean velocity field for U and W, according to the established Hit Rate metric. On the other hand, the higher moments are seemingly calculated with a sufficiently high precision. However, without a proper simulation of the velocity gradient, the moments can not be captured well by LES. To understand the nature of the problem, the scatter plots of measured and simulated values from LESa are shown in Figure 4.

The scatter plot between the PIVa and the LESa values in Figure 4a is located along the 1:1 line, though the absolute deviation A (dashed and dotted lines) for the streamwise velocity component is so small that most of the points do not fall in the prescribed region. Most of them fulfil only the relative deviation criterion D (dashed lines) in Figure 4a. This leads to a preliminary conclusion that the LES model fails in the prediction of the very low velocity values inside the canyon where small-scale vortices and intense shear exists, but it succeeds in the prediction of the fast velocity flow above the canyon.

The Hit rate scatter plot illustrates that the streamwise and vertical velocity components are subtly and moderately underestimated by the LESa according to Figure 4a,b, respectively. The momentum flux (Figure 4c) and the reduced TKE (Figure 4d) are predicted very well and reach a high Hit rate score. The additional discussion on the Hit rate results can be found in Section 6.

Table 4. Hit rate metric q.

Quantity	Full Street Canyon
U	0.59
W	0.36
$< u'w' >$	**0.83**
TKE	**0.83**

The bold values meet the acceptance criterion of **0.66** as defined in VDI [39] for each velocity component.
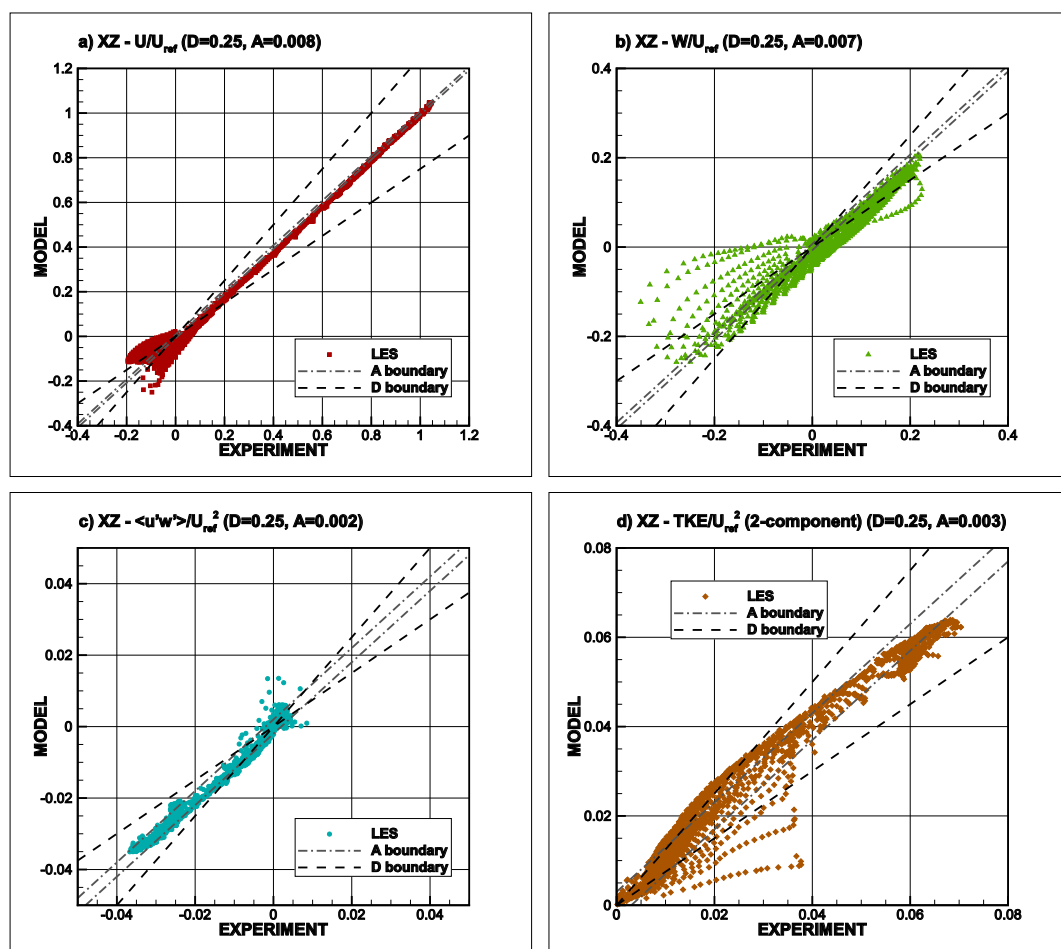

Figure 4. The Scatter plots of the measured (PIVa) and simulated (LESa) values obtained within the street canyon for the dimensionless (**a**) streamwise velocity; (**b**) vertical velocity; (**c**) momentum flux and (**d**) turbulent kinetic energy. Dashed lines denote the relative deviation D; dashed-and-dotted lines denote the absolute deviation A. 2400 points are plotted for each run.

4.3.2. Spatial Hit Rate

The STD of each quantity significantly differs from position to position in the street canyon due to the influence of long-term, large-scale flow structures on the stationarity of the data. For example, in our case, the values of the absolute deviation A, as derived from the STD of the streamwise velocity, exhibit a spatial scatter of $A(\mathbf{x}) \in (0.001 - 0.040)$ inside the rectangular area. The area where the

long-term structures occur (e.g., in the up-roof region) supposedly has a high STD, while the area of an intense small-scale mixing (e.g., canyon centre) exhibits low STD. If the measurement error is determined from a one-point measurement only, this reference point should be chosen with the utmost care.

To test the role of the space-dependent differences in the deviation criterion $A(\mathbf{x}) = A(x_i, z_i)$ for the validation, we included a particular measurement error into the Hit rate formula at each location separately as

$$q = \frac{1}{P} \sum_{i=1}^{P} q_i \quad \text{with} \quad q_i = \begin{cases} 1 & \text{for} \quad |\frac{M_i - E_i}{E_i}| \leq D \quad \text{or} \quad |M_i - E_i| \leq A(x_i, z_i) \\ 0 & \text{else} \end{cases} \tag{7}$$

The final *spatially sensitive* Hit rate agreement is shown in Table 5. The spatially sensitive Hit rate is supposed to be more precise since it reflects the spatial inhomogeneity of the flow. In our case, the spatial Hit rate on LESa is consistent with the standard Hit rate metric output. The larger $A(\mathbf{x})$ occurs mostly around the roof level, where velocities were predicted sufficiently well, and $A(\mathbf{x})$ remains small inside the canyon, where velocities were predicted poorly. Considering the fact that the rounding-off upward effect of the spatially averaged error $A = \overline{A(\mathbf{x})}$ poses less stringency on the Hit rate validation procedure in the inside-canyon area than a local $A(\mathbf{x})$, we found the standard Hit rate metric was resulting in slightly more optimistic results than the spatially sensitive Hit rate. Although the spatially sensitive Hit rate is considered by the authors of this paper as more precise, the standard single Hit rate validation metric does not deviate significantly in terms of results, and it is much more easily-applied. Hence, single Hit rate criterion is regarded as a suitable comparable tool for the comparison of a simulation with an experiment.

Table 5. Hit rate metric q without and with spatial sensitivity.

Quantity	LESa Standard	LESa Spatial
U	0.59	0.58
W	0.36	0.47
$< u'w' >$	**0.83**	**0.68**
TKE	**0.83**	**0.77**

The bold values meet the acceptance criterion of **0.66** as defined in VDI [39] for each velocity component.

4.4. Spectral Analysis

Both the TR-PIV experiment and the LES simulation have an advantage over the RANS and Gaussian models in providing the time-resolved data with a satisfactorily high temporal resolution, to which the spectral analysis is worth being applied. The power spectral densities were calculated as the square of the fast Fourier transformation of the streamwise velocity fluctuations time series. The resulting spectra were smoothed by non-overlapping rectangular blocks. The length of the blocks was exponentially increasing with the increasing frequency to get equidistant points on the logarithmic axis (about eight estimates per frequency decade). The comparison of the power spectral density obtained from the HWAc and the LESc time series at height $z/H = 2$ is shown in Figure 5. Contrary to the locations inside the street canyon, at this elevation Taylor's hypothesis on frozen turbulence can be considered. Above the reduced frequency of $n = fz/U = 0.1$, where f is the frequency, z is the elevation and U is the mean streamwise velocity component, there is agreement between the numerical and experimental data.

Since the LES is inherently limited for a correct simulation of the whole turbulent spectral range, it is, by definition, capable of simulating only *low-frequency ranges* and the *inertial subrange*, provided the grid resolution is high enough. The sub-grid vortices are only modelled ones, leading to the energy deficiency in the *high-frequency tail* of the spectral density plot ($n > 10$). Still, the LESc spectra follow

the well-known Kolmogorov $-2/3$ law ($-5/3$ in non-weighted representation), as depicted by the solid line in Figure 5.

On the *low-frequency tail* of the LESc spectra, the sudden drop in spectral energy at approximately $n = fz/U = 0.1$ is clearly notable in comparison with the dashed Karman's theoretical curve. The drop was detectable in all the LES canyons. With a LES periodic domain length of 16 H, only structures up to 8 H can be safely computed. However, structures of 16 H can exist and can in fact be very strong. The 8 H wave length corresponds with the dimensionless frequency $n = fz/U \approx 0.07$.
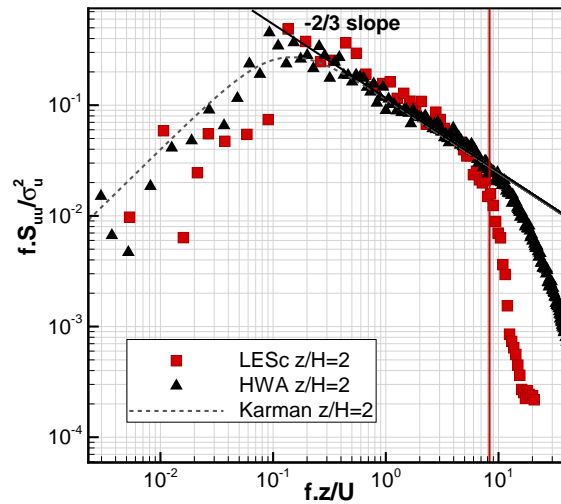

Figure 5. Comparison of the energy spectral density of the streamwise velocity at position $x/H = 0$, $z/H = 2$ for HWA (black triangles) and LESc (red squares). The solid black line represents the slope of the Kolmogorov $-2/3$ law, the dashed grey line represents the Karman's Theoretical curve. The solid vertical red line indicates the smallest scale not strongly affected by the sub-grid model and discretization errors with $\Lambda_{LES} \approx 0.24H = 12$ mm.

5. Results: Model Performance Assessment for Intermittent Flow

5.1. Quadrant Analysis

The quadrant analysis allows for a deeper insight into the dynamical behaviour of the flow, since it groups certain events based on their specific contribution to the total momentum flux, and provides their statistical overview. To be more specific, we obtain information about a particular contribution of the momentum flux $< u'w' >$ from the particular flux direction (i.e., quadrant) with the quadrant analysis. The definition of the quadrants, derived from the scatter plot of the streamwise and vertical velocity component fluctuations, was inspired by Willmarth and Lu [40]:

- $u' > 0, w' > 0$ - outward interaction (τ_1),
- $u' > 0, w' < 0$ - sweep (τ_2).
- $u' < 0, w' < 0$ - inward interaction (τ_3),
- $u' < 0, w' > 0$ - ejection (τ_4),

The particular contribution of the *i*-th quadrant τ_i to the total momentum flux $\tau_{xz} = < u'w' >$ is obtained from a formula of weighted average:

$$\tau_i = \frac{< u'w' >_i \cdot n_i}{N_{total}} \tag{8}$$

where $< u'w' >_i$ means the time-averaged momentum flux within the i-th quadrant, n_i is the number of events belonging to the i-th quadrant and N_{total} is the global number of events recorded during

the time period $t^*_{PIVa} = 1295$ and $t_{LESa}* = 1528$. The vertical profiles of the total momentum flux, $< u'w' >$, with each of the event contributions are plotted in Figure 6a. The total momentum flux is a simple sum of all the contributions.

First, it is worth pointing out that the peak shape (at $z/H = 1.1$) is quite different from the peak shape of the street canyons with the same aspect ratio, but with flat roofs (e.g., [7,25,41]). While the peak of the profile of the total momentum flux is narrow and located just above the roof-top of the street canyons with flat roofs, the pitched roofs generate a vertically more extensive shear layer and consequently produce a stronger exchange between the canyon cavity and the boundary layer aloft (for more details see [24]).

The quadrant analysis confirms that the sweep events (orange triangles in Figure 6a) and ejection events (green triangles in Figure 6a) clearly contribute the most to the total momentum flux, while the inward (light blue triangles in Figure 6a) and outward (dark blue triangles in Figure 6a) interactions are negligible. As the contribution of the sweep events is forecasted by LESa (solid lines) extraordinarily well in both the peak elevation and the magnitude above the roof top, the moderate over-estimation of the ejections leads to a slight over-prediction of the total momentum flux at the peak level. Again, the general tendencies of strong sweep and ejection events are predicted extremely well.

The momentum flux exhibits a significant diversion from the measured data in the lower part of the canyon ($z/H < 0.5$). The over-prediction by LESa is caused by a strong contribution from the inward interaction quadrant compared to the completely missing inward interaction in the case of PIVa. The LES with a grid resolution of 2 mm is probably unable to resolve the small-scale shear motion properly. The preliminary results from a finer grid resolution of the LES (1 mm) indicates much better agreement (not shown here).

Considering the hypothesis that a model, primarily, has to correctly simulate the momentum flux in order to predict velocity properly [18], the over-prediction of the inward interaction provides a possible explanation why the LESa fails to correctly predict the mean velocity profiles and 2-D fields, as presented in previous sections in Figures 2 and 3. Figure 6b reveals that the increase of the inward interaction significantly correlates with the flow pattern of the second POD mode calculated from LESa data, indicated by the red streamlines (the details are explained later in Section 5.3).

The sweep and ejection events often travel in a compact shape across the street canyon. For a better demonstration of these phenomena, it is convenient to plot their conditionally averaged shape as derived from several strong events. An example of a typical sweep from PIVc and a typical sweep from LESc, in the canyon, is presented in Figure 7a,b, respectively. The negative (orange) values denote the region where a strong sweep takes place whereas the positive (green) values denote the existence of a dominant ejection. Further, we evaluated the spatial distribution of each quadrant in the planar vector field xz by means of a spatially relative cumulative contribution $\varepsilon_i(t^*)$ from particular event $\tau_i(t^*)$ to the total momentum flux $\tau_{total}(t^*)$ according to the formula:

$$\varepsilon_i(t^*) = \frac{\tau_i(t^*)}{|\tau_{total}(t^*)|} \cdot 100\% \tag{9}$$

$$\tau_i(t^*) = \sum_{k=1}^{K} \sum_{l=1}^{L} \tau_{kl,i}(t^*) \tag{10}$$

$$\tau_{total}(t^*) = \sum_{k=1}^{K} \sum_{l=1}^{L} |\tau_{kl}(t^*)| \tag{11}$$

where $k = 1, 2...K$ and $l = 1, 2...L$ are the row and column numbers in the vector field, $|...|$ representing the absolute values of the inner product. The total momentum flux $\tau_{total}(t^*)$ in Equation (11) is the sum of absolute values from each quadrant at each time.
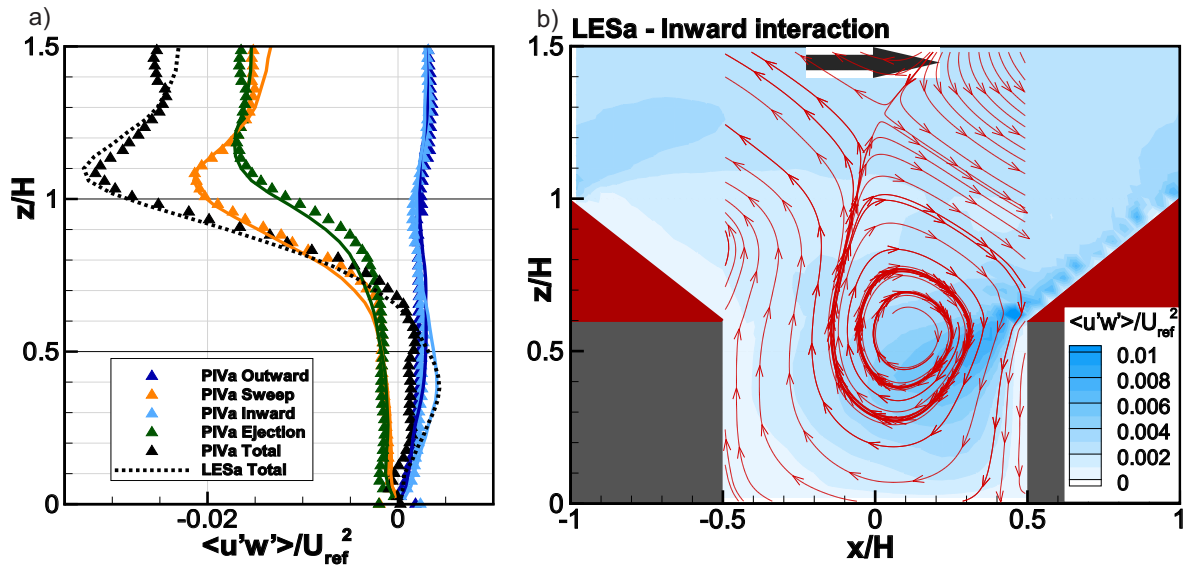
Figure 6. (**a**) The vertical profiles of the total vertical momentum flux and the particular event contributions to the total momentum flux from LESa (lines) and PIVa (triangles) at position $x/H = 0$. The colours correspond to the schematic diagram of the quadrant analysis in the bottom left corner in Figure 7; (**b**) 2D plane of the inward interaction from LESa (light blue contours) with the red streamlines of the second POD mode from LESa.
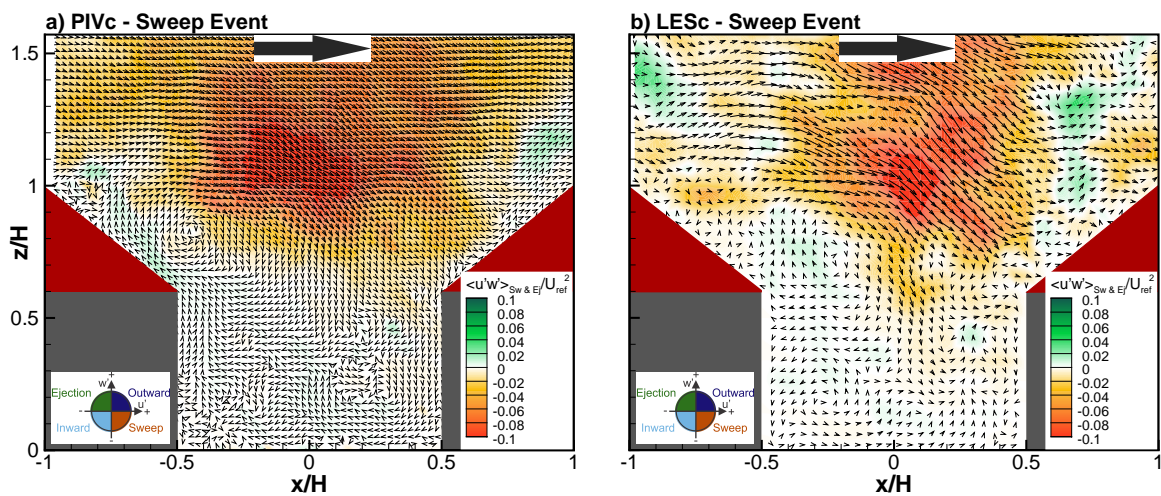

Figure 7. The characteristic examples of the sweep event (orange) at $y/H = 0$ for (**a**) PIVc and (**b**) LESc. A definition of the intensive events is explained in the following procedure and Figure 8.

The calculation of the contribution of the particular event $\varepsilon_i(t^*)$ from Equation (9) revealed that the sweep and ejection events occasionally represent up to $\varepsilon_{2,4}(t^*) > 80\%$ of the total momentum flux (see the red and green lines in Figure 8). Such a high contribution agrees with the many experimental and numerical studies dealing with the role of sweep and ejection in turbulent boundary layers (e.g., [40,42–44]). The specific time instants with $\varepsilon_2(t^*) > 80\%$ from the sweep quadrant serve as the data input for the conditional averaging of the momentum flux field in order to achieve a typical intensive sweep event in the canyon as shown in Figure 7.

The clear tendency for both events to pass the street canyon in an alternating fashion can be seen also in Figure 8a,b. This is supported by the large and negative value of the correlation coefficient between the relative contributions of sweeps and ejections, $R_{sw,ej} = -0.90$. When the sweep enters the canyon, the ejection is suppressed and vice versa. The frequency of such events occurring was analysed from the time series of their relative contribution $\varepsilon_i(t^*)$ defined by Equation (9). The mean

value derived from all instantaneous values $\varepsilon_i(t^*)$ was subtracted from the time series and the spectral function was obtained by the same algorithm used in the case of velocity fluctuations described as in Section 4.4. The spectra revealed that the characteristic frequency of this pseudo-wavy pattern occurs approximately at $fz/U = 0.2 \approx 6H$, taking into account an estimated convective velocity of the quadrant events [27] for both the PIVc and the LESc (Figure 9). The sweep and ejection events pass the canyon or are induced by the canyon geometry with the same pseudo-frequency and with the same relative intensity in both the experiment and the simulation. It is necessary to note that sweep and ejection events are not part of any vortex since their wavelength is larger than either the vertical or lateral dimension of the wind tunnel. In conclusion, the quadrant analysis proves that the LES is capable of reliably modelling large intermittent and organised structures in the flow above the obstacles.
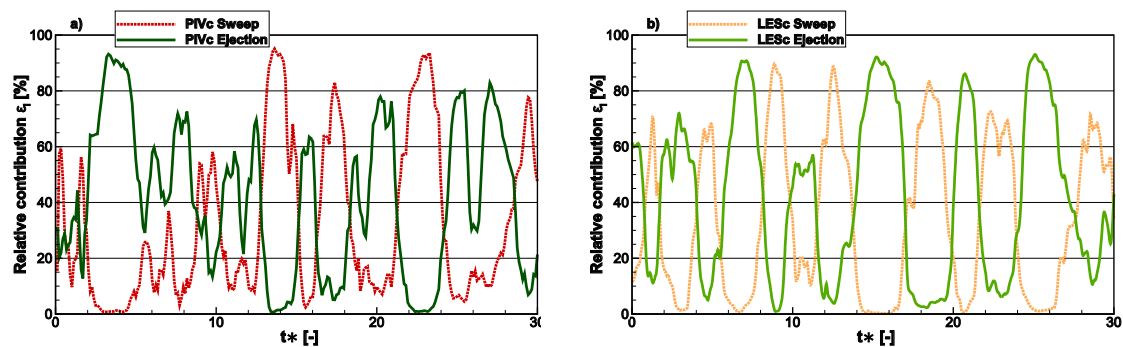

Figure 8. The segment with the time evolution of the sweep (red lines) and ejection (green line) relative contribution to the absolute total momentum flux for (**a**) PIVc and (**b**) LESc.
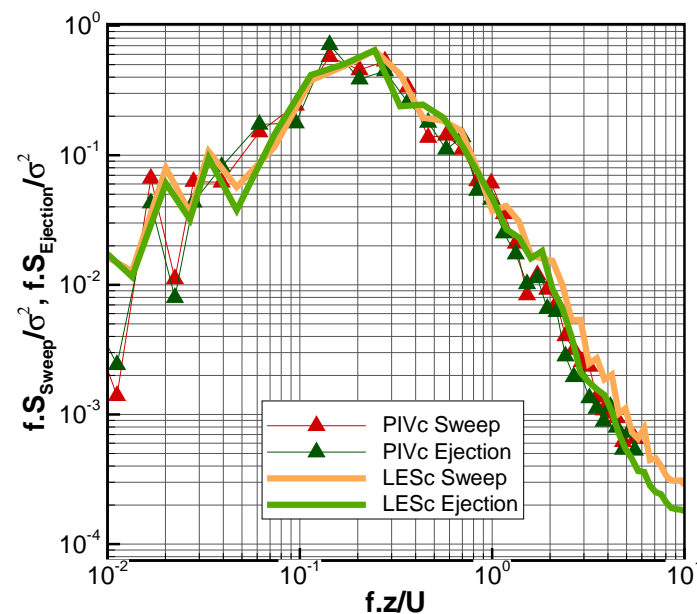

Figure 9. The spectral density plot of the relative contribution of the sweep and ejection events to the total momentum flux for PIVc (triangles) and LESc (lines).

5.2. Spatial Correlation

Spatial correlation helps to explore the link between transient flow dynamics across the field in a statistical sense. The normalised correlation coefficient at the point $\mathbf{x} + d\mathbf{x}$, where $\mathbf{x}$ is the reference point, was calculated according to formula

$$r_{uu}(\mathbf{x}, d\mathbf{x}) = \frac{1}{N-1} \sum_{i=1}^{N} \frac{u'(\mathbf{x}, t_i) u'(\mathbf{x} + d\mathbf{x}, t_i)}{\sigma_u(\mathbf{x}) \sigma_u(\mathbf{x} + d\mathbf{x})} \tag{12}$$

where N is the number of time-steps (snapshots) obtained from the continuous PIVc measurement and LESc simulation, and σ_u is the standard velocity deviation. For both PIVc and LESc vector fields, we calculated the correlation between the time series at the chosen reference point $\mathbf{x} = (x/H = 0, z/H = 1.25)$ and all other spatial locations. The correlation coefficients were calculated for velocity fluctuation u' and w', and for the momentum flux fluctuation $(u'w')'$. Since the spatial quadrant analysis (Section 5.1) reveals that appreciable regions of high momentum fluxes (i.e., the sweep and ejection events) pass the canyon, we aim to investigate the correlation between the time-series of these momentum fluxes $u'w'$ instead of a simple correlation between the quantity u' and w'. The contour-plots in Figure 10 display typical patterns of the spatial correlation above the street canyon similar to the one obtained in, e.g., Michioka et al. [7]. Regarding the qualitative comparison, the plots confirm a good agreement between the experimental (Figure 10a) and the numerical (Figure 10b) results.
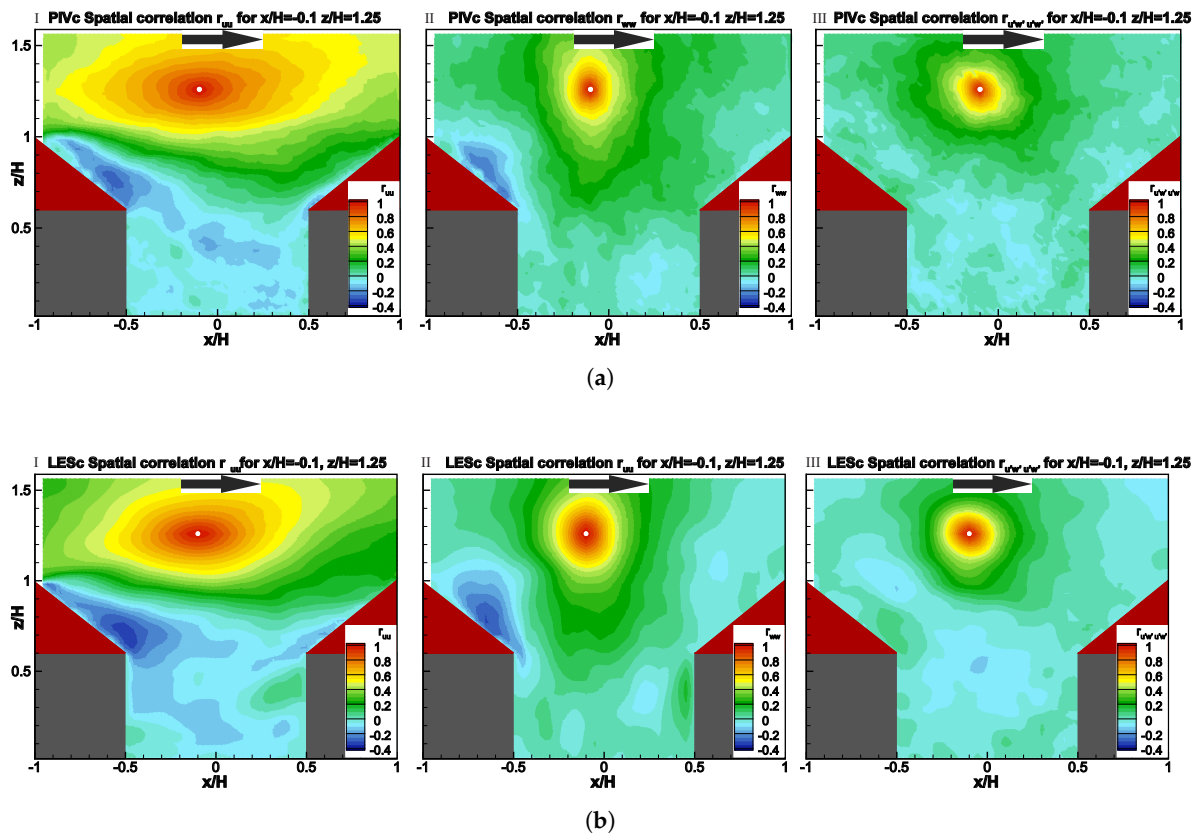

Figure 10. Spatial correlation of the normalised streamwise velocity fluctuation r_{uu} (first column), of the vertical velocity r_{ww} (second column) and of the fluctuation of the momentum flux $r_{u'w'u'w'}$ (third column) for the chosen point at $x/H = 0$, $z/H = 1.25$ for (**a**) PIVc and (**b**) LESc. The LES plot is interpolated onto the PIV grid (4977 points).

The contour-plots allow us to directly compare the correlation coefficient fields from the PIVc and LESc. To express the degree of similarity between the plots in Figure 10a,b, we calculated the *final correlation coefficient* via the following formula

$$R_{jj}(\mathbf{x}) = \frac{1}{P-1} \sum_{i=1}^{P} \frac{r_{jj,PIV}(\mathbf{x}, d\mathbf{x_i}) r_{jj,LES}(\mathbf{x}, d\mathbf{x_i})}{\sigma_{r_{jj,PIV}} \sigma_{r_{jj,LES}}} \tag{13}$$

where $P = 4977$ is the number of locations $\mathbf{x}$ in the measurement area and $j = u, w$ or $u'w'$.

The results of R_{uu}, R_{ww} and $R_{u'w'u'w'}$ obtained for the shared grid points of both PIVc and LESc (together 132 points) are plotted in Figure 11. The appropriate final correlation coefficient R_{jj} is presented by means of the coloured scale and is assigned to a specific location (square) within the investigated area. Figure 11 suggests that the greatest deviation in the LES predictions, compared with the experimental results, is located mainly inside the street canyon, close to the vicinity of the walls and near the canyon bottom, especially in the case of the momentum flux, $R_{u'w'u'w'}$. Again, the LESc apparently fails to predict the recirculation zone together with the small-scale structures within the canyon cavity, probably due to the coarseness of the grid resolution. Other lower correlations can be seen in the vicinity of the upstream building roof, where small-vortex shedding occurs. This, in accordance with previous results of the Hit rate validation metric, confirms that the transient dynamics, and consequently the ventilation processes, at these critical areas will not be predicted by the presented LES model in the proper manner.
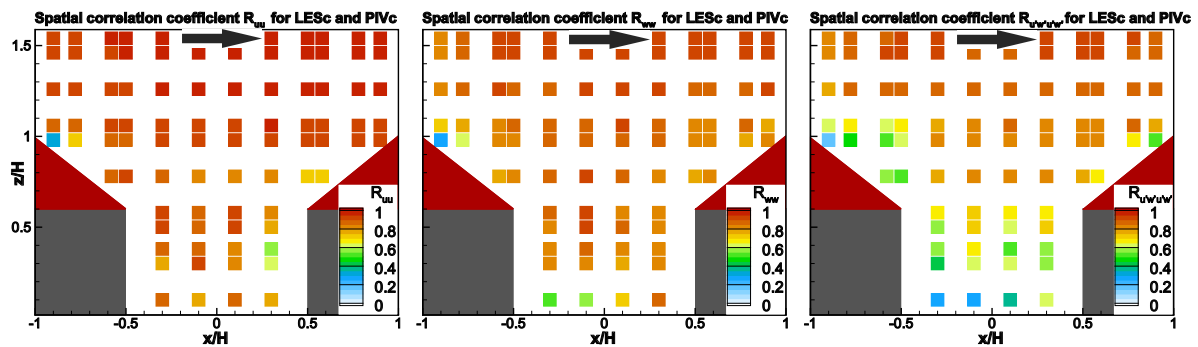

Figure 11. The final correlation coefficients between the PIVc and the LESc spatial correlation fields of the streamwise velocity R_{uu} (first column), of the vertical velocity R_{ww} (second column) and of the momentum flux $R_{u'w'u'w'}$ (third column). Each point shows the comparison based on the spatial correlation of the correlation coefficient fields between PIVc and LESc at one of the 132 shared points of the PIV and LES grids.

The range of the mean values of the correlation coefficient that corresponds to the individual canyons, and which is spatially-averaged over the entire investigated area within each canyon (always 132 shared points between the PIV and LES grids) for u, w and $u'w'$, are listed in Table 6. The relatively high unified values in Table 6 indicate that the correlation method for a single velocity component u or w is rather tolerant in measuring the degree of similarity between the predicted and observed short-time intermittent motions within the shear layer at the canyon bottom. In other words, this spatially-average single number from each canyon will not reveal the subtle differences between the measured and forecasted transient dynamics and will yield a rather high percentage of agreement. We presume that validations based solely on the spatially-averaged correlation of u and w would lead to an overestimation of the LES model with respect to the prediction of intermittent motions. However, the detailed picture of locally dependent final correlations, as depicted in Figure 11, is a suitable tool for the detection of problematic areas in the LES prediction.

Table 6. Final correlation coefficient spatially-averaged over the each canyon.

Quantity	LESc1-8
R_{uu}	0.92–0.94
R_{ww}	0.90–0.92
R_{uwuw}	0.82–0.85

5.3. Proper Orthogonal Decomposition

Contrary to a one-point spatial correlation, which simply carries out the statistical behaviour of the fluctuations with respect to one arbitrarily chosen reference point, the POD groups the correlated motions into contextual merit-based ensembles and thus provides a certain insight into the coherent intermittent dynamics [45]. Simply stated, for fluid mechanic applications, POD assembles the intermittent events together by finding their most appropriate representation (basal vectors). This representation expresses the highest TKE content in each vector from a statistical point of view. The POD may be applied for both the experimental data (e.g., [20,24,25,46]) and the data obtained from CFD simulations (e.g., [47]). Hence, it provides a valuable tool for comparing the results from numerical modelling with those from a physical experiment.

The POD was proposed by Lumley [48] as a tool for the detection of large coherent structures in the flow. This method is based on the assumption that we can extract special functions (alias basal vectors $\{\boldsymbol{\varphi}_m\}$) from the chaotic turbulent flow, those which possess the mathematical description of the coherent structures as the most probable flow features. It is thus possible to describe every value of the instantaneous velocity fluctuation at every instant of time and space $u'(\mathbf{x}, t)$ by a set of new basal vectors $\boldsymbol{\varphi}_p$ and their corresponding expansion coefficients a_p, where $p = 1, 2, \ldots 2P$ is equal to double the number of grid points P, as

$$u'(\mathbf{x}, t) = \sum_{p=1}^{2P} a_p(t)\boldsymbol{\varphi}_p(\mathbf{x}) \tag{14}$$

$$\boldsymbol{\varphi}_p^T \boldsymbol{\varphi}_q = \delta_{pq} \tag{15}$$

$$corr(a_p, a_q) = \delta_{pq} \tag{16}$$

where *corr* represents the correlation coefficient and δ_{pq} the Kronecker delta achieving value of 1 for $p = q$ and 0 otherwise.

The basis $\{\boldsymbol{\varphi}_p\}$ meets the orthogonality and normality criteria, so that the vectors $\boldsymbol{\varphi}_p$ (i.e., POD modes) are perpendicular to each other and are properly normalised. In the case of POD, this basis is not chosen *a priori* as in the Fourier or the wavelet analysis, but according to the input data. It is important to note that the POD modes are functions of space, not of time. The *p-th* eigenvalue λ_p corresponds to the *p-th* POD mode and contains information about the contribution of the *p-th* mode to the total turbulent kinetic energy (TKE). A reordering of the eigenvalues based on the descending TKE (and the ascending order of p)

$$\lambda_1 > \lambda_2 > \ldots > \lambda_{2P} \tag{17}$$

reveals the most dominant modes in the flow according to their relative contribution Π to the TKE [49]:

$$\Pi = \frac{\lambda_p}{\sum \lambda_p} * 100\% \tag{18}$$

We applied the POD to the horizontal and vertical velocity components inside a limited rectangular area of the street canyon. Data from both the LES and PIV were normalised by the reference velocity. Since the number of grid points obtained from PIV post-processing (2400 points) differs from the number of grid points in the LES simulation (1120 points), and also because the slightly different dimensions of the investigated areas (due to the different outer boundaries of the grids) might

cause certain differences in the POD results, we tested the sensitivity of the POD to these aspects first. We observed that it is better to keep the dimension of the region identical, irrespective of the differences in spatial resolution. It is also better to interpolate only the POD output, rather than the input data. Thus, every POD mode was calculated for the original grid, and then each LES mode $\boldsymbol{\varphi}_p$ was interpolated to the PIV grid.

In order to illustrate the spatial distribution of the modes $\boldsymbol{\varphi}_p$, the four most dominant POD modes for PIVa and LESa in terms of *TKE* are depicted in Figure 12a–d. It has to be emphasized that the black lines with the arrows, the so-called streamlines, were painted manually, hence their density and precise location serve for display purposes only.
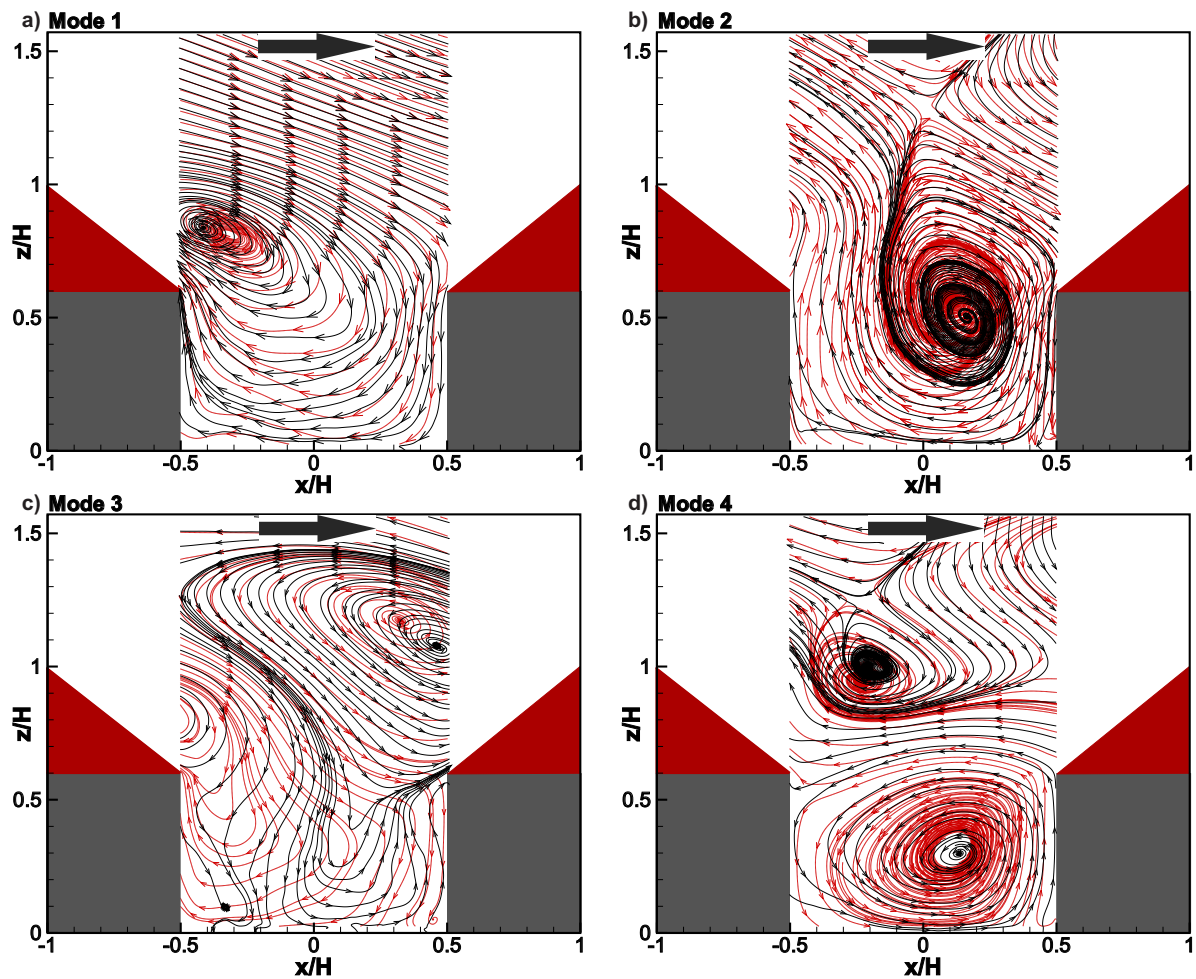

Figure 12. The POD modes for the restricted rectangular area within the street canyon for PIVa and LESa. (**a**–**d**) correspond to Mode 1–4. The black streamlines denote PIVa, the red streamlines denote LESa. The LESa modes are interpolated on the PIV grid.

The first mode in Figure 12a displays the vortex behind the roof, which is well pronounced and dominant in the case of the intermittent flow. Kellnerova et al. [24] proved that this vortex accurately captures the dominant street-canyon flow dynamics. The LESa version, involving the data from all of the simulated canyons, shows a good agreement with the PIV results with respect to the core of the vortex. This is a very important finding, since the first mode contributes the most (by 32%) to the total turbulent energy budget. The deviation of this roof-vortex core of PIVa from that of LESa ($\Delta x/H = 0.1$) can be considered small enough, resulting in an overall consistency of the modal shape and leading to a satisfactory validation.

Regarding the second mode (Figure 12b), the inflection point at the area above the roof is predicted precisely. The LES seems to push the center of the vortex between the walls. The recirculation vortex,

containing 7% of total TKE, is the main dynamical pattern responsible for the acceleration and deceleration of the mean recirculation vortex. The shape of the recirculation zone also moderately deviates from the experimental results since the LES enhances the backward flow near the downstream edge of the vortex. This backward flow contributes to the inward momentum flux (see Figure 6b) leading to an elevation and an inclination of the primary recirculation zone (see Figure 3a,b).

The third mode (Figure 12c) shows definite deviation from the experimental results concerning the curved trajectory of wind in the whole lower canyon. The LES's third mode further contributes to the inward interaction momentum flux in this area. Meanwhile, the other flow patterns, such as the vortices above the windward and leeward roof, are appropriately predicted. The fourth mode (Figure 12d), again, is very well forecasted.The fourth mode represents the late phase of the recirculation vortex, when the vortex is moving toward the ground. Although the latter two modes contribute only 6% and 4%, respectively, to the total TKE, Kellnerova et al. [24] showed that they occasionally play a significant role in street-canyon flow dynamics.

To evaluate the agreement between the simulated POD modes and the measured ones more clearly, the scatter plots for the first four dominant modes are displayed in Figure 13. The excellent similarity between the experiment and model for the streamwise and vertical velocity fluctuations, u'/U_{ref} and w'/U_{ref}, respectively, is further confirmed quantitatively by the Hit rate metrics results, and are listed in Table 7. The Hit rate score is evaluated in a similar way as in Section 4.3.1, i.e., the absolute deviation boundary A is taken as $A = 0.01$ and $A = 0.005$ for streamwise fluctuation and vertical fluctuation, respectively. These values of A are calculated as the mean standard deviation of corresponding velocity fluctuation. The only difference is that here, the member q_i in Equation (6) achieves a value of one when both the streamwise and vertical fluctuations satisfy the criteria for the streamwise and vertical deviation boundaries simultaneously.
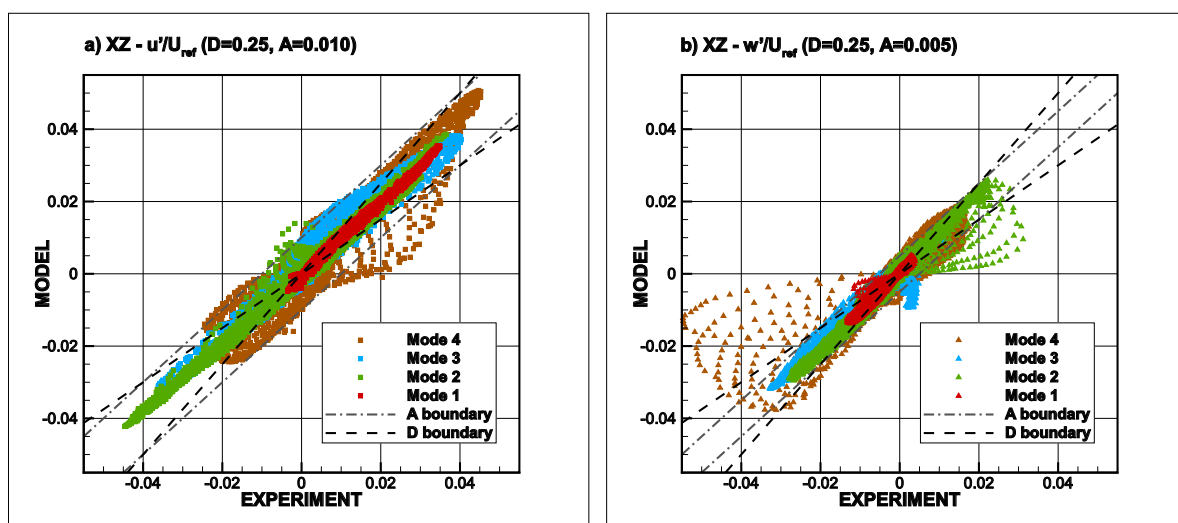

Figure 13. Scatter plots for modes 1-4 between the PIVa (experiment) and LESa (model) for (**a**) u'/U_{ref} and (**b**) w'/U_{ref}.

Table 7. Hit rate metric q for POD modes.

Quantity	Mode 1	Mode 2	Mode 3	Mode 4
u'/U_{ref} and w'/U_{ref}	**0.99**	**0.96**	**0.90**	**0.79**

The bold values meet the acceptance criterion of **0.66** as defined in VDI [39] for each velocity component.

Figure 14 displays the relative and cumulative contribution of each POD mode to the *TKE*. The relative contribution of the first mode calculated from all-the-canyons data (LESa), matched well with the experiment. Generally, in the case of higher modes, which mostly represent the vortices

inside the canyon, the LES predicts their systematically higher percentages of the contribution in terms of the turbulent kinetic energy. The LES forecast therefore exhibits a higher degree of coherency in correspondence with the faster rate of the cumulative contribution convergence. This indicates that the LES generates either a higher number of vortices or a higher rotational speed of the vortices within the recirculation zone compared to the experiment, especially in connection with the vortex associated with the second and third POD mode. Incidentally, Figure 6b illustrates the close relationship of the second POD mode with the inward interaction. The stronger second and third modes in LES consequently enhance the inward interaction of the momentum flux at the lower part of the canyon, thereby leading to a higher positive total momentum flux (the third column in Figure 3) and a streamwise inclined recirculation pattern (the first and the second column in Figure 3) that modifies the velocity profiles in the lower canyon part (Figure 2a).
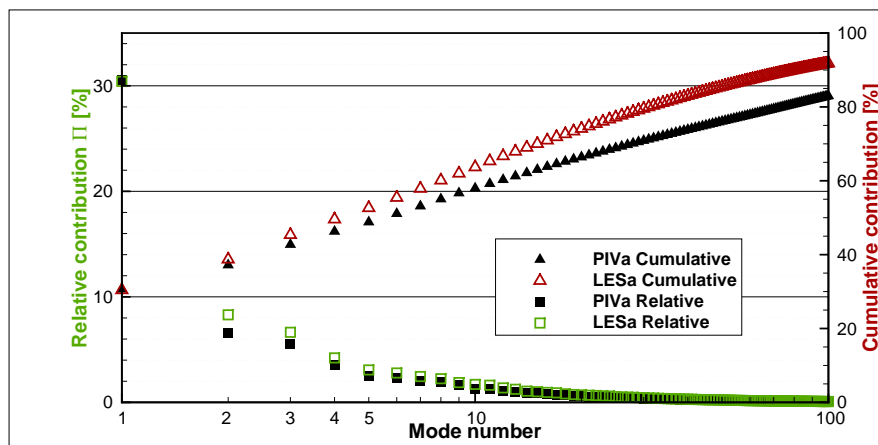

Figure 14. The comparison of the relative (squares) and cumulative (triangles) contributions of the first 100 individual POD modes of PIVa and LESa to the *TKE*.

6. Discussion on Validation Metrics

Since the general validation metrics Section 4.3 are originally proposed for the concentration data, the velocity data easily comply with their criterion thresholds. As mentioned previously, we therefore propose for the Pearson correlation coefficient to increase the acceptance criterion to 0.9, instead of 0.8.

The Hit rate metric points out issues encountered while using a PIV measurement technique for a street-canyon model topology. Firstly, the Hit rate benefit lies in a simple implementation of the measurement error, as obtained from repeated measurements at a well-chosen reference position or in the investigated region. With the PIV and other multi-points techniques, however, it might be difficult to achieve a sufficiently high number of repetitive runs, while maintaining a sufficiently long acquisition time. Hence, the results from the Hit rate method should not be regarded as the "benchmark" validation metric before the PIV runs provide enough repetitive data. Near-wall areas, where the PIV post-processing is likely to substitute a large portion of spurious vectors, have to be cautiously dealt with.

Secondly, the Hit rate is extremely sensitive to the magnitudes of the preselected data. In our case, the relative deviation boundary, $D = 0.25$, is a much less stringent criterion than the absolute deviation boundary, as determined from a very low experimental uncertainty. If the data are selected from locations containing only large values (above the roof area, for example), the majority of the data fits into the relative deviation limits. This factor can be effectively demonstrated for the above-roof region $(-0.5 < x/H < 0.5, 1 < z/H < 1.5)$ with large values of the streamwise velocity, U, the momentum flux and reduced turbulent kinetic energy, and with almost negligible vertical velocity, W. The final Hit rate score achieves a value of 1 for U/U_{ref}, TKE/U_{ref}^2 and $< u'w' > /U_{ref}^2$, seemingly suggesting

the ideal model situation. On the other hand, the vertical velocity component, W/U_{ref}, achieves an extremely low value of 0.20, indicating a rather poor LES performance (see the left column in Table 8).

Table 8. Hit rate metric q.

Quantity	Above-Roof Region	Windward Region
U	**1.00**	0.52
W	0.20	**0.75**
$< u'w' >$	**1.00**	**0.68**
TKE	**1.00**	**0.85**

The bold values meet the acceptance criterion of **0.66** as defined in VDI [39] for each velocity component.

In the region containing a small streamwise velocity component, U, and the large quantities, W, TKE, and $< u'w' >$, as in the windward region of the canyon ($0.25 < x/H < 0.5$, $0.25 < z/H < 1$), the results would be different. The Hit rate score would achieve high values for W/U_{ref}, TKE/U_{ref}^2 and $< u'w' > /U_{ref}^2$, while the streamwise component U/U_{ref} would not satisfy the threshold criterion (see the right column in Table 8). The result suggests that the validation technique should employ data from all the possible locations available from both the experimental and numerical output.

Hypothetically, when using precise measurement techniques in a well-controlled experiment (ensuring a low uncertainty), a fast-motion flow region would always comfortably satisfy the Hit rate relative criterion, whereas a slow-motion flow region would hardly meet the low experimental uncertainty. An absolute deviation criterion depending on the precision of the measurement technique that varies from study to study may make the inter-studies comparison of the Hit rate scores problematic. It might be more practical to pose one unified absolute deviation criterion A in the form of a percentage (e.g., 2% of the nominal velocity, $A = 0.02U_{ref}$).

7. Conclusions

The advanced validation procedures were performed, and others introduced, in order to compare the time-resolved LES simulations with the time-resolved PIV measurements on street-canyon topology. The validation procedure followed the general procedures recommended by Schatzmann et al. [15], Cox and Tikvart [38], which employ time-space averaged statistics. Further, an innovative approach based on coherent detection methods was implemented to compare the predicted and observed values of both the intermittent large- and small-scale features in the flow.

The general metrics, encompassing the time-space averaged data, were fulfilled for all the tested quantities. The LES performance failed to satisfy the minimum Hit rate criterion (0.66) in both the mean streamwise and vertical velocity components, while the quantities based on the fluctuations provided a satisfactory agreement. The strengths and weaknesses of the Hit rate metric were thoroughly discussed.

The large-scale structures in the up-roof area were predicted accurately, in contrast to the small-scale vortices near the street-canyon bottom-area. The discrepancies between the modelled and the measured mean velocities at the bottom area, where a strong shear takes place, are apparently associated with the deviation in the momentum flux.

The advanced validation techniques, the quadrant analysis together with POD, revealed that the enhanced inward interaction in the case of the LES simulation is associated with a more intensive vortex formation inside the canyon. Further, the quadrant analysis shows that the dominant flow structures in the up-roof region - the strong sweep and ejection events - have similar compact shapes and pass through the street canyon with identical frequency and intensity in both the simulation and the experiment. The detailed Fourier spectral analysis revealed an undefined drop of energy in LES in the energy-containing range across the entire time domain. Nevertheless, the inertial subrange was modelled extraordinarily well. Finally, the POD demonstrated that the shape of the coherent structures from the LES is strikingly similar to the shape of the observed structures. The Hit rate metrics applied to the POD modes showed an excellent agreement. The turbulent kinetic energy contained in the most

dominant LES structure was identical with the measured one, while the less dominant LES structures exhibited a slightly more turbulent kinetic energy. This suggests that the simulated flow is more organised and less noisy than the flow observed in the experiment.

In an ideal case, the tested model should pass all the available validation metrics. However, in the real situation we might need to prioritize some metrics over others to prove satisfactory model performance in given applications. In our study we focused on the flow within an urban roughness layer, where the dynamical exchange of pollution and heat is a crucial factor. The dominant momentum events, which are correlated with heat and emission transport [50,51], can be quite easily described by the quadrant analysis in terms of contribution to TKE and their spectral characteristics, and we recommend to use it. The quadrant analysis can be executed either as one-point method or spatial multi-point analysis, as drafted in this paper.

If the synchronised multi-points data are at disposal, the POD would be a quick and useful tool to compare the large structures, both visually and numerically. On the other hand, using a spatial correlation might overestimate the LES performance with respect to the simulation of intermittent motions.

The validation methods presented, including the coherent detection methods, proved to be an indispensable tool for the proper validation of the time-resolved numerical codes. The analysis of the coherent features helped us to easily validate, qualitatively and quantitatively, the prediction against the observation, as well as to explain their possible contradictions. We demonstrated that although the modelling of sub-grid, small-scale structures inside a street canyon did not meet the Hit rate validation criteria, the dominant dynamics of the larger scale can be modelled in a satisfactory manner.

Author Contributions: R.K. researched the literature, designed the experiment, developed the code for coherent structured detection methods, executed the calculations and wrote the paper. V.F. performed the LES simulation. V.U. installed the PIV system and performed the experiment. K.J., Š.N. and H.C. suggested the type of the utilised methods, discussed the results and provided feedback for both the velocity and concentrations data. Z.J. supervised the project and corrected the paper.

Abbreviations

The following abbreviations are used in this manuscript:

AIJ	Architectural Institute of Japan
CFD	Computational Fluid Dynamics
COST	European Cooperation in Science and Technology
CTA	Constant Temperature Anemometry
DNS	Direct Numerical Simulation
EPA	Environmental Protection Agency
HWA	Hot-Wire Anemometry
LES	Large Eddy Simulation
PIV	Particle Image Velocimetry
POD	Proper Orthogonal Decomposition
RANS	Reynolds-averaged Navier–Stokes
STD	Standard Deviation
TKE	Turbulent Kinetic Energy
VDI	Verein Deutscher Ingenieure (The Association of German Engineers)

Appendix A. TR-PIV System Description

An overview of the PIV parameters is listed in Table A1.

Table A1. Parameters of the TR-PIV.

Laser	Peagus-PIV-Diode-Pumped (Dual Head) Nd:YLF
Beam diameter	1.5 mm
Repetition rate	100 & 2 × 500 Hz
Illuminated Area	100 × 100 mm
Energy per cavity (at 1 kHz)	10 mJ
Camera sensor resolution	1280 × 1024 pxs
Interrogation area	32 × 32 pxs
Overlapping	50% (80 × 64 = 5120 vectors)
Final spatial resolution	1.2 × 1.2 mm
Acquisition time	16.3 s & 2 × 3.27 s = 22.7 s
Number of snapshots N	3 × 1634 = 4902
Grid points/reduced grid points P	4977/2400

Appendix B. LES Model Description

For the LES model CLMM, the filtered Navier-Stokes equations, with an eddy-viscosity sub-grid, and the continuity equations are considered in the present study as

$$\frac{\partial \bar{u}}{\partial t} + \nabla \cdot (\bar{u}\bar{u}) = -\nabla \bar{P} + \nabla \cdot (\nu_{\text{eff}} \nabla \bar{u}) + f_i, \tag{A1}$$

$$\nabla \cdot \bar{u} = 0, \tag{A2}$$

where the overbar represents the filtered quantity, u is the velocity vector, $\bar{P} = \bar{p}/\rho + \frac{2}{3}k_r$ is the modified pressure, $\bar{p}$ is the pressure and $k_r = \frac{1}{2}\text{Tr}(\tau) = \frac{1}{2}\text{Tr}(\overline{uu} - \bar{u}\bar{u})$, defined using the trace of the subgrid stress tensor τ, is the subgrid kinetic energy. As a knowledge of p and k_r is not needed, only the modified pressure is computed during the solution. The effective viscosity ν_{eff} in Equation (A1) is the sum of the kinematic viscosity ν and the sub-grid scale (SGS) eddy viscosity ν_{sgs}. The last term in Equation (A1), f_i, is the constant volume force representing the pressure gradient driving the flow. The value of f_i was determined by previous coarser resolution tests so that the reference time-averaged velocity is close to the experiment. The sub-grid scale eddy viscosity is computed by the σ-model from Nicoud et al. [32]

$$\nu_{\text{sgs}} = (C_\sigma \Delta)^2 \frac{\sigma_3 (\sigma_1 - \sigma_2)(\sigma_2 - \sigma_3)}{\sigma_1^2}, \tag{A3}$$

where $\sigma_1 \geq \sigma_2 \geq \sigma_3 \geq 0$ are the singular values of tensor $\nabla \bar{u}$, Δ is the filter width and C_σ is an empirical model constant. The value $C_\sigma = 1.35$ was used for the present computations.

The coupling of the velocity and pressure fields is performed using the fractional step (pressure correction) method from Brown et al. [52]. The time integration is based on the 3-stage Wray's Runge-Kutta method [53].

Appendix C. Measurement Uncertainty Assessment

Firstly, we attested the representativeness of each PIV run by means of a convergence plot (not shown). The convergence plots of the streamwise and vertical velocity were calculated as the relative deviation of the time-averaged velocity over the gradually increasing time interval from the time-averaged velocity over the entire measurement duration. We evaluated the maximum deviation from the mean velocity value after the inclusion of 75% of the snapshots.

The convergence plots verified that 1634 snapshots are a reasonable, but still minimum, number of snapshots for a reliable PIV performance with a maximum deviation from the mean velocity magnitude value of approx. 2% for both velocity components, U/U_{ref} and W/U_{ref}, 8% for the momentum flux,

$< u'w' > /U_{ref}^2$, and 7% for the reduced turbulent kinetic energy, TKE/U_{ref}^2. Thus, we can conclude that the PIVc runs lasting for 3.2 s contain a sufficiently high number of representative flow events for the intermittent flow analysis. The same holds true for the LES performance, as the maximum deviation from the mean velocity magnitude value of both velocity components quickly achieves a low error percentage of 2%, the momentum flux of 13% and TKE of 8% after reaching 10,000 samples. The performance of LES with 10,000 snapshots for each canyon is therefore considered to be adequate for the validation of flow dynamics.

We also performed the sensitivity test to an acquisition time by comparing the mean values point-by-point between the individual runs. Using the Frobenius norm, we compared the mean velocities, the standard deviations and reduced TKE. The averaged deviation of the mean velocity between all three runs was 2.6% for the streamwise component and 5.5% for the vertical component. The standard deviation had a scatter of 11% and 6% for the U-component and W-component, respectively. Also, the difference for reduced TKE was only 3%. All results can be found in [27].

Further, the POD modes from individual runs were compared by means of the Frobenius norm. The first POD modes derived from the individual runs did not deviate more than 4.2% from each other. The results for other modes are published in [27].

These values were considered to be sufficiently low enough to assume that even a short measurement, lasting for 3.2 s and assembling 1634 snapshots, captures a representative number of the dominant transient features in the flow. Therefore, we collected all three runs together and performed the statistics introduced in this paper. Some advanced statistics are not sensitive to the sampling frequency, for example the POD, when the essential dynamics in the flow is captured by the snapshots. For the spectral characteristics, where either the sampling frequency or continuity of the data are crucial, only the continuous data from the 500 Hz run were used.

Generally, the repetitions of the measurements involve all the possible random variations in an experimental performance—the switching off of the facility (e.g., a wind tunnel) and the devices (e.g., a laser and a particle seeding generator). The measurement also involves a bias error caused by both the PIV system and the post-processing procedure (the presence of spurious vectors, a strong gradient velocity field, a sub-pixel interpolation, a pixel-locking effect). The authors considered the bias error to be notably greater than the random error. Since we were unable to estimate the type of hypothesised distribution of the velocity mean values, we just simply calculated the standard deviation as a true error uncertainty, which presumably involves both types of error.

References

1. Casey, M.; Wintergerste, T. *Best Practice Guidelines—ERCOFTAC Special Interest Group on Quality and Trust in Industrial CFD*; COST: Brussels, Belgium, 2000.
2. Oberkampf, W.L.; Trucano, T.G. Verification and validation in computational fluid dynamics. *Prog. Aerosp. Sci.* **2002**, *38*, 209–272. [CrossRef]
3. Schatzmann, M.; Leitl, B. Issues with validation of urban flow and dispersion CFD models. *J. Wind Eng. Ind. Aerodyn.* **2011**, *99*, 169–186. [CrossRef]
4. Moonen, P.; Gromke, C.; Dorer, V. Performance assessment of Large Eddy Simulation (LES) for modeling dispersion in an urban street canyon with tree planting. *Atmos. Environ.* **2013**, *75*, 66–76. [CrossRef]
5. Soulhac, L.; Perkins, R.J.; Salizzoni, P. Flow in a Street Canyon for any External Wind Direction. *Bound.-Lay. Meteorol.* **2008**, *126*, 365–388. [CrossRef]
6. Salizzoni, P.; Soulhac, L.; Mejean, P. Street canyon ventilation and atmospheric turbulence. *Atmos. Environ.* **2009**, *43*, 5056–5067. [CrossRef]
7. Michioka, T.; Sato, A.; Takimoto, H.; Kanda, M. Large-Eddy Simulation for the Mechanism of Pollutant Removal from a Two-Dimensional Street Canyon. *Bound.-Lay. Meteorol.* **2011**, *138*, 195–213. [CrossRef]
8. Soulhac, L.; Salizzoni, P.; Mejean, P.; Perkins, R. Parametric laws to model urban pollutant dispersion with a street network approach. *Atmos. Environ.* **2013**, *67*, 229–241. [CrossRef]
9. Mirzaei, P.A.; Carmeliet, J. Dynamical computational fluid dynamics modeling of the stochastic wind for application of urban studies. *Build. Environ.* **2013**, *70*, 161–170. [CrossRef]

10. Soulhac, L.; Salizzoni, P.; Mejean, P.; Didier, D.; Rios, I. The model {SIRANE} for atmospheric urban pollutant dispersion; {PART} II, validation of the model on a real case study. *Atmos. Environ.* **2012**, *49*, 320–337. [CrossRef]

11. Hofman, J.; Samson, R. Biomagnetic monitoring as a validation tool for local air quality models: A case study for an urban street canyon. *Environ. Int.* **2014**, *70*, 50–61. [CrossRef] [PubMed]

12. Hofman, J.; Lefebvre, W.; Janssen, S.; Nackaerts, R.; Nuyts, S.; Mattheyses, L.; Samson, R. Increasing the spatial resolution of air quality assessments in urban areas: A comparison of biomagnetic monitoring and urban scale modelling. *Atmos. Environ.* **2014**, *92*, 130–140. [CrossRef]

13. Franke, J.; Hellsten, A.; Schlunzen, H.; Carissimo, B. The Best Practise Guideline for the CFD simulation of flows in the urban environment: Quality Assurance of Microscale Meteorological Models. In Proceedings of the Fifth International Symposium on Computational Wind Engineering. Chapel Hill, NC, USA, 23–27 May 2010.

14. Franke, J.; Hellsten, A.; Schlünzen, H.; Carissimo, B. *COST 732 Quality Assurance and Improvement of Microscale Meteorological Models—The Best Practise Guideline for the CFD Simulation of Flows in the Urban Environment*; COST Action 732; COST: Brussels, Belgium, 2007.

15. Schatzmann, M.; Olesen, H.; Franke, J. *COST 732 Model Evaluation Case Studies: Approach and Results—Quality Assurance of Microscale Meteorological Models*; COST Action 732; COST: Brussels, Belgium, 2010.

16. Franke, J.; Hirsch, C.; Jensen, A.; Krus, H.; Schatzmann, M.; Westbury, P.; Miles, S.; Wisse, J.; Wright, N. Recommendations on the use of CFD in Wind Engineering. In Proceedings of the International Conference on Urban Wind Engineering and Building Aerodynamics: COST C14—Impact of Wind and Storm on City life and Built Environment. Rhode-Saint-Genese, Belgium, 5–7 May 2004.

17. Tominaga, Y.; Mochida, A.; Yoshie, R.; Kataoka, H.; Nozu, T.; Yoshikawa, M.; Shirasawa, T. AIJ guidelines for practical applications of CFD to pedestrian wind environment around buildings. *J. Wind Eng. Ind. Aerodyn.* **2008**, *96*, 1749–1761. [CrossRef]

18. Jimenez, J.; Moser, R.D. *A Selection of Test Cases for the Validation of Large-Eddy Simulations of Turbulent Flows*; The North Atlantic Treaty Organization: Washington, DC, USA, 1998.

19. Westerweel, J.; Elsinga, G.E.; Adrian, R.J. Particle Image Velocimetry for Complex and Turbulent Flows. *Ann. Rev. Fluid Mech.* **2013**, *45*, 409–436. [CrossRef]

20. Hertwig, D.; Leitl, B.; Schatzmann, M. Organized turbulent structures: Link between experimental data and LES. *J. Wind Eng. Ind. Aerodyn.* **2011**, *99*, 296–307. [CrossRef]

21. Hertwig, D.; Patnaik, G.; Leitl, B. LES validation of urban flow, part I: Flow statistics and frequency distributions. *Environ. Fluid Mech.* **2017**, *17*, 521–550. [CrossRef]

22. Hertwig, D.; Patnaik, G.; Leitl, B. LES validation of urban flow, part II: Eddy statistics and flow structures. *Environ. Fluid Mech.* **2017**, *17*, 551–578. [CrossRef]

23. Hertwig, D. On Aspects of Large-Eddy Simulation Validation for Near-Surface Atmospheric Flows. Ph.D. Thesis, University of Hamburg, Hamburg, Germany, 2013.

24. Kellnerova, R.; Kukacka, L.; Jurckova, K.; Uruba, V.; Janour, Z. PIV measurement of turbulent flow within a street canyon: Detection of coherent motion. *J. Wind Eng. Ind. Aerodyn.* **2012**, *104–106*, 302–313. [CrossRef]

25. Perret, L.; Savory, E. Large-Scale Structures over a Single Street Canyon Immersed in an Urban-Type Boundary Layer. *Bound.-Lay. Meteorol.* **2013**, *148*, 111–131. [CrossRef]

26. Blackman, K.; Perret, L.; Savory, E. Effect of upstream flow regime on street canyon flow mean turbulence statistics. *Environ. Fluid Mech.* **2015**, *15*, 823–849. [CrossRef]

27. Kellnerova, R. Wind-tunnel Modelling of Turbulent Flow Inside the Street Canyon. Ph.D. Thesis, Charles University in Prague Faculty of Mathematics and Physics, Prague, Czech Republic, 2014.

28. Fuka, V. PoisFFT—A free parallel fast Poisson solver. *Appl. Math. Comput.* **2015**, *267*, 356–364. [CrossRef]

29. Kim, J.; Kim, D.; Choi, H. An Immersed-Boundary Finite-Volume Method for Simulations of Flow in Complex Geometries. *J. Comput. Phys.* **2001**, *171*, 132–150. [CrossRef]

30. Peller, N.; Duc, A.L.; Tremblay, F.; Manhart, M. High-order stable interpolations for immersed boundary methods. *Int. J. Numer. Methods Fluids* **2006**, *52*, 1175–1193. [CrossRef]

31. Morinishi, Y.; Lund, T.; Vasilyev, O.; Moin, P. Fully conservative higher order finite difference schemes for incompressible flow. *J. Comput. Phys.* **1998**, *143*, 90–124. [CrossRef]

32. Nicoud, F.; Toda, H.B.; Cabrit, O.; Bose, S.; Lee, J. Using singular values to build a subgrid-scale model for large eddy simulations. *Phys. Fluids* **2011**, *23*, 085106. [CrossRef]

33. VDI. *Physical Modelling of Flow and Dispersion Processes in the Atmospheric Boundary Layer—Application of Wind Tunnels*; VDI 3783, Part 12; Verein Deutcher Ingenieure: Dusseldorf, Germany, 2000.

34. Xie, X.; Huang, Z.; Wang, J.S. Impact of building configuration on air quality in street canyon. *Atmos. Environ.* **2005**, *39*, 4519–4530. [CrossRef]

35. Kastner-Klein, P.; Berkowicz, R.; Britter, R. The influence of street architecture on flow and dispersion in street canyons. *Meteorol. Atmos. Phys.* **2004**, *87*, 121–131. [CrossRef]

36. Pascheke, F.; Barlow, J.F.; Robins, A. Wind-tunnel Modelling of Dispersion from a Scalar Area Source in Urban-Like Roughness. *Bound.-Lay. Meteorol.* **2008**, *126*, 103–124. [CrossRef]

37. Takano, Y.; Moonen, P. On the influence of roof shape on flow and dispersion in an urban street canyon on the influence of roof shape on flow and dispersion in an urban street canyon. *J. Wind Eng. Ind. Aerodyn.* **2013**, *123*, 107–120. [CrossRef]

38. Cox, W.M.; Tikvart, J.A. A statistical procedure for determining the best performing air quality simulation model. *Atmos. Environ. Part A Gen. Top.* **1990**, *24*, 2387–2395. [CrossRef]

39. VDI. *Environmental Meteorology—Prognostic Microscale Windfield Models—Evaluation for Flow around Buildings and Obstacles*; VDI 3783, Part 9; Beuth Verlag: Berlin, Germany, 2005.

40. Willmarth, W.W.; Lu, S.S. Structure of the {R}eynolds stress near the wall. *J. Fluid Mech.* **1972**, *55*, 65–92. [CrossRef]

41. Cui, Z.; Cai, X.; Baker, C.J. Large-eddy simulation of turbulent flow in a street canyon. *Q. J. R. Meteorol. Soc.* **2004**, *130*, 1373–1394. [CrossRef]

42. Robinson, S.K. Coherent Motions in the Turbulent Boundary Layer. *Ann. Rev. Fluid Mech.* **1991**, *23*, 601–639. [CrossRef]

43. Kanda, M.; Moriwaki, R.; Kasamatsu, F. Large-Eddy simulation of turbulent organized structures within and above explicitly resolved cube arrays. *Bound.-Lay. Meteorol.* **2004**, *112*, 343–368. [CrossRef]

44. Coceal, O.; Dobre, A.; Thomas, T.G.; Belcher, S.E. Structure of Turbulent Flow Over Regular Arrays of Cubical Roughness. *J. Fluid Mech.* **2007**, *589*, 375–409. [CrossRef]

45. Aubry, N.; Guyonnet, R.; Lima, R. Spatiotemporal Analysis of Complex Signals: Theory and Applications. *J. Stat. Phys.* **1991**, *64*, 683–739. [CrossRef]

46. Hilberg, D.; Lazik, W.; Fiedler, H.E. The Application of Classical POD and Snapshot POD in a Turbulent Shear Layer with Periodic Structures. *Appl. Sci. Res.* **1994**, *53*, 283–290. [CrossRef]

47. Sen, M.; Bhaganagar, K.; Juttijudata, V. Application of proper orthogonal decomposition (POD) to investigate a turbulent boundary layer in a tunnel with rough walls. *J. Turbul.* **2007**, *8*, 1–21. [CrossRef]

48. Lumley, J.L. *The Structure of Inhomogeneous Turbulent Flows*; Yaglom, A.M., Tatarski, V.I., Eds.; Nauka: Moscow, Russia, 1967; pp. 166–178.

49. Nobach, H.; Tropea, C.; Cordier, L.; Bonnet, J.P.; Delville, J.; Lewalle, J.; Farge, M.; Schneider, M.K.; Adrian, R.J. *Springer Handbook of Experimental Fluid Mechanics*; Tropea, C., Yarin, A., Foss, J., Eds.; Springer: New York, NY, USA, 2007; pp 1337–1398.

50. Christen, A.; van Gorsel, E.; Vogt, R. Coherent structures in urban roughness sublayer turbulence. *Int. J. Climatol.* **2007**, *27*, 1955–1968. [CrossRef]

51. Nosek, Š.; Kukačka, L.; Kellnerová, R.; Jurčáková, K.; Jaňour, Z. Ventilation Processes in a Three-Dimensional Street Canyon. *Bound.-Lay. Meteorol.* **2016**, *159*, 259–284. [CrossRef]

52. Brown, D.L.; Cortez, R.; Minion, M.L. Accurate Projection Methods for the Incompressible Navier–Stokes Equations. *J. Comput. Phys.* **2001**, *168*, 464–499. [CrossRef]

53. Spalart, P.R.; Moser, R.D.; Rogers, M.M. Spectral methods for the Navier-Stokes equations with one infinite and two periodic directions. *J. Comput. Phys.* **1991**, *96*, 297–324. [CrossRef]